To the Graduate Council:

I am submitting herewith a dissertation written by Hung-Chih Li entitled "Molecular Modeling of Perfluoro Compounds." I have examined the final paper copy of this dissertation for form and content and recommend that it be accepted in partial fulfillment of the requirements for the degree of Doctor of Philosophy, with a major in Chemical Engineering.

H D Cochran

Hank D. Cochran, Major Professor

We have read this dissertation
and recommend its acceptance:

Acceptance for the Council:

Vice Provost and Dean of
Graduate Studies

Molecular Modeling of Perfluoro Compounds

A Dissertation

Presented for the

Doctor of Philosophy

Degree

The University of Tennessee, Knoxville

Hung-Chih Li

May 2002

Copyright © 2002 by Hung-Chih Li

All rights reserved.

DEDICATION

This dissertation is dedicated to my parents, Tshy-Lang Lee and Yu-Chih Lee, for always supporting my decision no matter what and being there for me when needed, and life itself, for I would not be here or anywhere without it.

ACKNOWLEDGMENTS

I wish to thank all those who helped me in the completing Doctor of Philosophy in Chemical Engineering. I thank Dr. Cochran for his guidance and support without which I would not have a chance to work on this project. I thank Dr. Cummings for his suggestions and guidance regarding molecular modeling and mathematics. I also thank Dr. Collier and Dr. Van Hook for serving in my committee and providing valuable insights and suggestions. Last but not least, I thank Dr. Cui and Dr. McCabe for their help in all aspects.

I thank my family, my friends, and my colleagues, whose encouragement made this work possible.

ABSTRACT

Perfluoro compounds receive much attention due to their distinctive properties and multiple applications. Consequently, it would be of great interest to be able to model those applications with molecular simulation techniques. To achieve this goal, a realistic potential model is needed. For perfluoroalkanes, such a model has been developed and reported. However, for perfluoroethers, no such model currently exists. In the first part of this work, a preliminary model, based on *ab initio* calculations and Gibbs ensemble phase equilibrium calculations, was developed for a single perfluoroether, perfluoromethylpropylether; this work has been accepted for publication. Then, using the above methods plus an extension of the Gibbs-Duhem integration method, a realistic united atom potential model has been developed and then optimized using all available vapor-liquid phase equilibrium data for perfluoroethers. This model is composed of a harmonic function for the bond bending potential, a 7^{th} order polynomial function of cosine ϕ for the torsional potential, partial charge, and Columbic interaction for the long-range interaction, and Lennard-Jones potential for van der Waals interaction. This model has been shown to reproduce the phase envelope and the critical properties of the perfluoroethers reasonably well. During the development process, *ab initio* calculations for all modeled molecules were done to provide the intramolecular force field as well as the partial charge for the electrostatic potential. The results of the *ab initio* calculations also provide insight into the static and dynamic molecular structures which might be helpful in understanding the behavior of

the perfluoroethers later in the applications of this potential model. In this work, the Gibbs-Duhem integration technique has been extended to the development a potential model for a set of complex molecules. This application could automate the process of parameterization in potential model development, which is currently carried out by trial and error. A generalized partial charge set is also suggested for perfluoroether chain molecules.

Also, following previous work by Salaniwal et al. on the self-assembly of water and surfactant in super- or near-critical carbon dioxide with a di-chain surfactant having one perfluoroalkane chain, the normal component of the pressure tensor and interfacial tension have been calculated. This work attempted an extension of a method developed for pure fluids to a complex mixture; however, the results were problematic and further work is needed.

With the potential model developed in this work, a similar simulation of a reverse micelle system could be carried out with perfluoroethers as surfactants. This system would be of more interest to industry since perfluoroethers are stable in water unlike the surfactant in the previous simulation, a perfluoroalkane. Also, this potential model could be used to study the lubrication with perfluoroethers by calculating the viscous properties of target perfluoroether under shear; such a study is currently underway. Although, with a united atom model, quantitative reproduction of experimental transport properties could not be expected, simulations with this potential model should provide useful qualitative insights.

For dynamic properties, sometimes united atom potential model is not enough to reproduce the experimental data correctly as in the previous application, and an explicit-

atom model is required. Base on the experience in this work, developing and testing of such model would be the work next in line. The *ab initio* results of this work could be used directly in such an effort. For an explicit-atom model, comparison against spectroscopic data from experiment would be a useful tool to refine such a model.

TABLE OF CONTENTS

Chapter 1 Background and Objectives 1

1.1 Applications of perfluoroethers 1

1.2 Potential model development 5

1.3 Objectives 10

Chapter 2 Calculation Methods 12

2.1 Potential model development 12

2.1.1 Electronic structure calculations 12

2.1.2 Gibbs ensemble Monte Carlo simulation 17

2.1.3 Gibbs-Duhem Integration 20

Chapter 3 Results and Discussion 23

3.1 Results of *ab initio* calculations 24

3.1.1 Geometry optimization 24

3.1.2 Dihedral energy profile and torsional potential 36

3.1.3 Partial charges 49

3.2 Fitting Lennard-Jones parameters to phase diagrams 59

Chapter 4 Conclusions and Recommendations 73

Bibliography 76

Appendices 84

Appendix A Molecular dynamics simulations of reverse micelles 85

A.1 Method 85

A.2 Implementation of pressure profile calculation.....90

A.3 Pressure profile and interfacial tension.....93

A.4 Conclusions and recommendations for the reverse micelle work.....101

Appendix B Implementation and application of Gibbs-Duhem integration.....103

Vita 109

LIST OF TABLES

Table 1. Optimized geometry parameters.....37

Table 2. Critical properties of the modeled molecules.....70

Table 3. Parameters of the potential model for perfluoroethers.....71

LIST OF FIGURES

Figure 1. Diagrams of the modeled molecules, perfluoroethylmethylether, perfluoromethylpropylether, and perfluorodimethoxymethane.....25

Figure 2. Schematic of the grouping of the united atom, and the assigning of the two dihedral angles.....26

Figure 3. Diagram of the optimized structure of perfluoroethylmethylether and schematic representations of the structure.....29

Figure 4. Comparison of optimized structures of perfluoroethylmethylether and perfluoro-normal-butane.....30

Figure 5. Diagram of the optimized structure of perfluoromethylpropylether and schematic representations of the structure.....33

Figure 6. Diagram of the optimized structure of perfluorodimethoxymethane and schematic representations of the structure.....35

Figure 7. Energy profile and torsional potential model for dihedral angle, C-C-C-O in perfluoroethylmethylether.....39

Figure 8. Energy profile, torsional potential model, and schematic representations for dihedral angle, C-C-C-O in perfluoromethylpropylether.....41

Figure 9. Comparison of the energy profiles of dihedral angle C-C-O-C in perfluoromethylpropylether and perfluoroethylmethylether.....43

Figure 10. Energy profile, torsional potential model and schematic representations for dihedral angle, C-C-C-O in perfluorodimethoxymethane.....44

Figure 11. Comparison of the energy profiles of dihedral angle C-O-C-O in perfluorodimethoxymethane rotating in two different directions.....46

Figure 12. Comparison of the energy profiles of all three different dihedral angles...48

Figure 13. Explicit atom partial charge profile on rotation around dihedral angle C-C-C-O for perfluoromethylpropylether calculated by the RHF method with the cc-pvdz basis set.....50

Figure 14. United atom partial charge profile along dihedral angle C-C-C-O for perfluoromethylpropylether calculated by the RHF method with the cc-pvdz basis set.....52

Figure 15. Weighted united atom partial charge profile along dihedral angle C-C-C-O for perfluoromethylpropylether calculated by the RHF method with the cc-pvdz basis set.....54

Figure 16. Weighted united atom partial charge profile along dihedral angle C-C-O-C for perfluoromethylpropylether calculated by the RHF method with the cc-pvdz basis set.....55

Figure 17. Weighted united atom partial charge profile along dihedral angle C-C-O-C for perfluoroethylmethylether calculated by the RHF method with the cc-pvdz basis set.....57

Figure 18. Weighted united atom partial charge profile along dihedral angle C-O-C-O for perfluorodimethoxymethane calculated by the RHF method with the cc-pvdz basis set.....58

Figure 19. Phase diagram of perfluoromethylpropylether from simulation with first parameter set and experiment.....60

Figure 20. Phase diagram of perfluoroethylmethylether from simulation with first parameter set and experiment.....61

Figure 21. Phase diagram of perfluoromethylpropylether from simulation with the final parameter set and experiment.....64

Figure 22. Phase diagram of perfluoroethylmethylether from simulation with the final parameter set and experiment.....65

Figure 23. Phase diagram of perfluorodimethoxymethane from simulation with the final parameter set and experiment.....68

Figure A-1. Definitions of contour, C_{ij} in the Irving-Kirkwood and Harasima pressure tensors.....88

Figure A-2. Schematic representation of $\mathbf{e}_{\phi}^{(i)}$ and $\mathbf{e}_{\theta}^{(i)}$ 91

Figure A-3. Density and pressure tensor profiles for system with surfactant.....94

Figure A-4. Density and pressure tensor profiles for system without surfactant.....96

Figure A-5. Comparison of P_n pressure profile for systems with and without surfactant.....98

Figure A-6.. P_n pressure profile from simulation and Pt calculated from Pn for systems with surfactant.....99

Figure A-7. P_n pressure profile from simulation and Pt calculated from Pn for systems without surfactant.....100

CHAPTER 1

BACKGROUND AND OBJECTIVES

1.1 Applications of perfluoroethers

In the past decade, perfluoroethers have attracted interest from a wide range of communities because of their importance in a number of applications and research areas. Perfluoropolyethers, and perfluorocompounds in general, have a unique combination of physical and chemical properties which makes them suitable for a wide range of potential applications in the medical, biotechnology, electronic, and oil and gas industries [1, 2].

Perfluoropolyethers are generally unreactive, non-toxic, non-flammable fluids, making them excellent candidates as high performance lubricants [3-5]. For example, Fomblin® and Krytox® are widely used as lubricants for magnetic recording media because of their low vapor pressure, oxidative stability, and relatively stable structures [6-8]. A number of theoretical and experimental studies have been focused on the physical properties and chemical reactions of these molecules in applications such as hard disk drive lubrication. In 2000, for spin-off and static friction (or striction), Nakakawaji et al. [9] reported the dependence on the average molecular weight of the

lubricants. Spin-off is a problem due to high-speed rotation of the disc, smaller spacing between discs, and temperature rising, etc. They reached the conclusion that the number average molecular weight should be higher than 2000 to avoid the spin-off and lower than 6000 to reduce the striction. Waltman [10] used *ab initio* and experimental methods to study the mobile state of the lubricants and the interaction of the lubricants with the carbon surface. In his paper, he reported the energy barrier for rotation about bonds between the backbone atoms as well as the torsional potentials. He concluded that rotation around the C-O bond has a lower energy barrier than that around the C-C bond; hence, lubricants with more C-O bonds (in this case, Zdol®) are more flexible.

As with many other polymer building blocks, numerous monomers or oligomers of perfluoropolyethers have been used in block copolymers to adjust the properties of the product [11-15]. One of the important properties of perfluorinated compounds is their extremely low intermolecular interaction, which accounts for many of their distinctive properties, including the low surface tension. For example, the surface tension of perfluoropolyethers is around 20–22 mN/m [11], which is much lower than that of hydrocarbon polymers. By using perfluoropolyethers to form block copolymers with hydrocarbon polymers, the surface properties of the polymer can be adjusted [11] which is of great interest to industry. Toselli et al. [11] measured the thermal and surface properties of the poly(ε-caprolactone)-poly(fluoroalkylene oxide)-poly(ε-caprolactone) block copolymers with different fractions of fluoroalkylene oxide (perfluoropolyether), and showed that the hydrophobicity depends on the concentration of the hydroxy groups on the copolymers, which is a function of the changing molecular

weight (number molecular weight (g/mol) in their case), because with fixed poly(ε-caprolactone) length, the longer the polymer is the smaller the fraction of poly(ε-caprolactone) will be and hence the smaller concentration of the hydroxy group. With this, polymers with selective adhesive properties can be designed. Additionally Thanawala and Chaudhury modified the surface properties of a poly(dimethylsiloxane) elastomer by reacting a perfluorinated ether to the siloxane network [12]. This operation significantly reduced the surface energy of the polymer without affecting the bulk properties of the polymer.

In the pharmaceutical, biomedical, and biotechnology industries, perfluoropolyethers have also attracted attention because of their chemical and bio-chemical inertness in addition to other distinctive properties, which when combined with their high solubility of oxygen and other respiratory gases, has led to a number of applications, such as, blood plasma substitutes, eye fluid, infusion fluid in the treatment of burns, and in cosmetics [2]. For example, Pantini et al. [16] tested Fomblin HC® as an additive in the treatment of dermatitis and reported a highly successful result due to the protective effect of Fomblin HC® against water and oil soluble substances. Johnson et al. [17] studied the cell growth of several different types of cell on polymer networks composed of perfluoropolyethers and indicated the potential applications as biomaterials in related areas. However, there are some concerns regarding the toxicity of perfluoropolyether compounds in particular applications [18, 19]; therefore, extra care should be taken for such applications.

Additionally, several simple perfluoroethers can be used as potential chlorofluorocarbon (CFC) substitutes [20]. When CFCs were discovered to be the major cause of the formation of the ozone hole, a tremendous research effort was carried out to find alternative substances. Several simple perfluoroethers such as perfluoromethylpropylether and perfluorodimethoxymethane have received attention as potential CFC substitutes [20] because they are inert and relatively benign to the environment. Van Hook and his group conducted a series of experiments on simple perfluoroether molecules [20, 21] and reported their thermodynamic properties such as phase equilibrium densities and vapor pressures in order to evaluate them to replace CFCs. The phase equilibrium properties are among the few experimental data sets that are available in the open literature for perfluoroethers.

A particularly topical application is the possible use of functionalized perfluoropolyethers as surfactants that can form microemulsions which disperse water in supercritical carbon dioxide [22-24], helping to make CO_2 a more versatile replacement solvent in the chemical and related industries. In 1996, Johnston et al. [23] used several spectroscopic techniques to verify the existence of water cores inside reverse micelles formed by an ammonium carboxylate perfluoropolyether with average molecular weight of 740. They also showed that protein molecules, bovine serum albumin (BSA), dissolved in the water core have similar spectroscopic properties as those dissolved in buffer solution at pH = 7.0 mimicking the pure water. This showed that the aqueous environment inside the reverse micelles is similar to that of bulk water, which is important for reactions such as enzymatic reactions. Eastoe et al. [25] also observed the

formation of reverse micelles with a water core in near-critical carbon dioxide with a di-chain surfactant, $[(C_7F_{15})(C_7H_{15})CHSO_4^-Na^+]$. Recently, by molecular dynamics simulation, Salaniwal et al. [26] showed the self-assembly of the same surfactant at the same thermodynamic state as Eastoe's work. However, the perfluoroalkane surfactant used in Eastoe's system is not thermodynamically stable. It decomposes in water. Therefore, it would be more interesting to study Johnston's and/or Beckman's [24] surfactants with molecular simulation. To reproduce the thermodynamic properties of a system accurately, a realistic potential model is needed. However, there is no such model presently available for perfluoroethers.

1.2 Potential model development

For molecular simulations including molecular dynamics, Monte Carlo, and molecular mechanics, choosing an appropriate potential model or force field is one of the most important steps to achieve realistic results from the simulations because molecular simulation results are exact in terms of statistical mechanics up to the limit of the method/algorithm and the potential model utilized. There are several different approaches for developing potential models. Depending on the application and the target molecule, the potential model for a molecule could be simple and transferable or very complicated and specific. For some common and important molecules such as water [27-29] and carbon dioxide [30], it is necessary to develop a specific potential model for them. However, for members of a homologous series such as alkanes or perfluoroalkanes etc., transferable and expandable set of parameters is usually sought.

Therefore, it is common practice to parameterize potential models for some basic building blocks and 'train' the parameter set to cope with the target molecules and applications. In the rest of this section, some existing force fields based on the idea of transferable parameters and the approaches used to build up the force field will be introduced.

Amber [31, 32], originally a program for model building, has evolved into a software package that is capable of performing molecular mechanics, molecular dynamics, and Monte Carlo simulations and has other modern features such as quantum mechanic/ molecular mechanic (QM/MM) hybrid simulation methods. Amber has become arguably one of the most commonly used molecular simulation packages, especially in the fields related to bio-molecules. The force fields that are adopted in Amber [33-35], referred to as Amber force fields, are applied in many other software packages such as MacroModel®. The Amber force fields include intramolecular terms such as bond stretching, bond bending, torsional, and improper terms (to keep the branched molecule from inverting) as well as the non-bonded terms such as van der Waals and electrostatic interactions as shown in equation (1). In some cases, particularly for biological systems, hydrogen bond and polarization terms are included, if necessary. The total energy V_{total} is given by

$$V_{total} = \frac{1}{2}\sum_{bonds} K_r (r - r_0)^2 + \frac{1}{2}\sum_{angles} K_\theta (\theta - \theta_0)^2 + \frac{1}{2}\sum_{dihedrals} K_\phi [1 + \cos(n\phi - \delta)] + \sum_{non\text{-}bonded} \left(\frac{A_{ij}}{R_{ij}^{12}} - \frac{Bij}{R_{ij}^{6}} + \frac{q_i q_j}{4\pi\varepsilon_0 R_{ij}} \right) \quad (1)$$

where the first and second terms are the harmonic stretching and bending potentials, the third term is the torsional potential, and the last term is the non-bonded term.

In the Amber force field, both united atom (where a segment is a group of atoms not a single atom) and explicit atom (where all atoms in a molecule are explicitly modeled) models of the simulated molecules are available. Similar to the concept behind the group contribution methods, in united atom models, sites that constitute a molecule are assigned as different atom types according to their composing atoms, electron configuration, and in some cases, their neighboring atoms. For a target molecule, each site and/or a group of sites is compared to the existing database of atom types and assigned a set of parameters if matched. If the parameters do not exist for a particular type, a series of procedures for developing the parameters set is suggested.

First of all, the equilibrium structure parameters subscripted 0 in equation (1), are either obtained from experimental data or derived from *ab initio* electronic structure calculations. Then, the corresponding constants are derived from normal mode analysis, which can be done also with *ab initio* electronic structure calculations. Usually, thermodynamic properties do not depend on the intramolecular potentials very much, especially the stretching and bending terms. Therefore, values from other similar molecules or standard values, for example 109.5^{o} for sp^3 bond angle, can be applied for parameters in these two terms as long as transport or spectroscopic properties are not the desired properties. For derivation of the torsional potential, an energy profile along the particular dihedral angle should be constructed with partial geometry optimization by *ab initio* electronic structure calculation. Then the resulting profile should be used to fit a

functional form, which accounts for the torsional potential. In Amber force fields, atomic point charges are used for the electrostatic potential. To derive the point charges, an electrostatic potential surface is generated with electronic structure calculations and then used to fit the partial charges on each site. Finally, the remaining parameters, the Lennard-Jones parameters, are obtained by comparing simulation results with experiment data. In this work, mostly the same procedures have been followed, and hence they will be discussed in detail later in Chapter 2.

OPLS (optimized potentials for liquid simulations) is another commonly used potential model developed by Jorgenson's group. Originally, OPLS was proposed with a partial united atom expression (only hydrogen atoms on aliphatic carbons are implicit) [36-39], and was extended to include the explicit aliphatic hydrogen atoms because of the additional flexibility provided for the charge distribution and the torsional energetics [40]. OPLS has a similar functional expression to Amber, and it is common practice in the literature to take the parameters for intramolecular potentials from Amber and combine them with the non-bonded parameters from OPLS [39]. The force fields so obtained are normally identified as Amber/OPLS. One very important concept in OPLS is that a force field intended for the use in fluid simulations involving liquid should be tested against experimentally determined liquid properties to ensure the correct descriptions of the non-bonded interactions, and hence the name OPLS.

CHARMM (Chem. at HARvard Macromol. Mechanics) [41] is another very popular program for the modeling of macromolecules. Like Amber, the term CHARMM later referred to the force field as well. The CHARMM force field [41-43]

has a slightly different approach toward deriving the force field parameters. The intramolecular force field terms for CHARMM are similar to those seen in equation (1) with the addition of an extra harmonic Urey-Bradley term to account for in-plane deformations and separate symmetric and asymmetric bond stretching modes. The approach to obtaining the intramolecular force field parameters is also similar to that applied in Amber. To obtain the partial charges, atomic charges obtained from Mulliken population analysis [44] are used as the initial guess, and then the partial charges are adjusted to fit the interaction energy, geometry, and dipole moment of a model system including the model compound and the solvent. After the atomic partial charges are derived, heat of vaporization and molecular volume of the condensed phase are used to adjust van der Waals parameters.

In addition to Amber, OPLS, and CHARMM, there are several other widely adopted force fields such as CVFF [45], MMFF [46], etc. They all share a common point: they are all developed for and applied mostly to bio-molecules. As mentioned before, the appropriate choice of force field depends on the application because of the database that is used to 'train' the model. For molecular simulations of phase coexistence and/or other condensed phases, it is more important that the model can properly describe the intermolecular interaction over a wide range of thermodynamic state points such as temperature and pressure. Gibbs ensemble Monte Carlo simulation [47] provides a useful tool to simulate phase equilibrium, which naturally spans a range of temperature or pressure, and hence is becoming a crucial addition to the methods used in potential model development for deriving the van der Waals parameters.

1.3 Objectives

In this work, two objectives have been pursued. The primary objective was to develop a potential model that is suitable for the molecular simulation of liquid perfluoroethers, especially for the calculation of the thermodynamic properties of the condensed phase. The primary objective has been successfully achieved. A secondary objective was to use molecular dynamics simulation to further examine the reverse micelle system that was previously simulated, especially to determine the pressure inside the water core and the surface tension between the micelle and the solvent however, a particularly difficult situation was encountered in the secondary objective regarding the pressure profile calculation. The results, at this time, have not been validated. Therefore, to maintain the integrity of the dissertation, all the materials related to the reverse micelle simulation have been moved to appendix A.

In section 1.1, many applications of perfluoroethers and perfluoropolyethers have been described. It would be of great value to be able to model perfluoropolyethers with molecular simulation techniques. Generally it is well recognized that the applicability of a potential model or force field lies in its parameterization. Hence, in order to obtain accurate predictions of the thermophysical properties of perfluoroethers from simulation, it is necessary to develop an accurate potential model that is fitted to liquid state thermodynamic properties in addition to *ab initio* calculations. In this work, approaches that are mentioned in section 1.2 were used to develop a united atom potential model for the molecular simulation of perfluoroethers in their condensed phase, which will make realistic molecular simulations of such compounds possible.

The proposed potential model was first developed, based on the phase envelope of a single perfluoroether, perfluoromethylpropylether, and has been accepted for publication. Based on that model and additional *ab initio* calculations for other modeled molecules, a more generalized potential model has also been developed. The *ab initio* calculation results themselves are of interest because the information obtained from them could help understand the properties of the perfluoroethers. This generalized potential model makes possible realistic simulations for applications of perfluoroethers. As a matter of fact, the potential model for perfluoroethers developed in this work is now applied to the calculation of viscous properties of perfluoroethers which is important for their applications in lubrication.

In addition, Gibbs ensemble techniques were adapted and used for phase equilibrium simulations of perfluoroethers, and Gibbs-Duhem integration techniques (described below) were extended and used for simultaneous optimization of potential model parameters for several perfluoroether molecules against their experimental vapor-liquid phase equilibrium data. The Gibbs-Duhem integration techniques are also shown to be a tool to improve the efficiency for parameter optimization and to automate the optimization process.

CHAPTER 2

CALCULATION METHODS

2.1 Potential model development

The proposed force field for perfluoroethers consists of bond angle bending terms E_{ba}, a torsional term $E_{torsion}$, and terms to describe the van der Waals, E_{vdW}, and electrostatic interactions E_{es}, with the total energy being given by the sum of these contributions:

$$E = E_{ba} + E_{torsion} + E_{vdw} + E_{es} \quad (2)$$

In the parameterization of this force field, three different types of calculation were performed, *ab initio* quantum mechanical calculations, classical Gibbs ensemble Monte Carlo simulations [47], and Gibbs-Duhem integration calculation [48].

2.1.1 Electronic structure calculations

Geometry optimization and single point energy calculation: Electronic structure calculations are used to obtain the optimized geometry of the target molecule, which provides us with equilibrium bond lengths, bond angles, and dihedral angles. All the calculations are performed exclusively with Gaussian 98® [49] using the restricted

Hartree-Fock method and the cc-pvdz basis set (RHF/cc-pvdz). For single point energy calculations, the second order Möller-Plesset, MP2, method is applied with the same basis set.

Bond stretching and bond bending: As in many other united atom models [50-52], the bond lengths in this model are fixed at their equilibrium positions, and bending potentials are described by simple harmonic functions of the form:

$$E_{ba} = \sum_{\text{angles}} K_{\theta}\left(\theta - \theta_{eq}\right)^2 \tag{3}$$

where θ is the bond angle. The equilibrium bond angles, θ_{eq}, are obtained by geometry optimization calculations and then each bond angle is perturbed from its equilibrium value while keeping the rest of the geometry parameters fixed. The energy difference between the perturbed and equilibrium geometry is calculated and used to infer the bond-bending constant, K_{θ}.

Torsional potentials: When parameterizing the torsional potential of chain molecules, the independence between different dihedral angles is a common simplifying assumption. However, with this assumption the resulting potential model will not necessarily reproduce the *ab initio* results in terms of optimized geometries. Since the model being developed in our work is focused on applications to phase equilibrium, this is not expected to have a significant impact, and hence independence of the dihedral angles is assumed. To obtain the torsional potentials, partial optimizations on the geometry of the molecule are carried out to generate the potential energy as a function of dihedral angle. During this process, the target dihedral angle is frozen at a

predetermined value, and the remaining degrees of freedom in the molecule are allowed to relax. This approach is justified because the torsional motions have lower frequencies than the bending motions; so, the other atoms should be allowed to adjust to the change in dihedral angle. To obtain the potential energy profile, such partial optimizations are performed for each dihedral angle from 0^o to 180^o in increments of 15^o. The resulting potential energy profile for each dihedral angle, ϕ, is then fitted to a 7^{th} order polynomial equation in cosine(ϕ) as follows:

$$E_{torsion} = \sum_{Di} \sum_{j=0}^{7} a_{Di,j} \cdot \cos^{j}(\phi) \tag{4}$$

where D_i identifies dihedral angles.

Partial charges: The determination of partial charges is more complicated than the other terms in the force field because the partial charge is not a measurable property that can be obtained directly by operating on the wave functions. Population analysis methods such as the Mulliken method [44] tend to generate unreliable results because of the simplifications used in such methods and can be, in the case of Mulliken charges, very basis-set dependent [53]. An alternative approach is to fit the point charges at pre-selected positions to the electrostatic potential surface generated by *ab initio* calculation [33, 34, 54, 55]. The partial charges thus obtained can be very conformation-dependent because of the statistical ill-behavior of deeply-buried charges [56] since the closest predetermined grid points to the buried sites are generally closer to other sites. Hence, it could require a significant change in the resulting partial charges on those buried sites just to achieve a small improvement in the optimization. However, neglecting the

conformational dependence of the partial charges can lead to severe error in properties such as free energy in a molecular simulation [57]. One way to circumvent this problem, while accounting for the conformational variance in partial charges, is to carry out the fitting process at several different conformations and then weight the resulting partial charges using Boltzmann statistics [58], and this is the approach applied in this work. Another way is to restrict the partial charges to a targeted set of charges or to a set of charges that can reproduce a desired property such as the dipole moment generated by *ab initio* calculation at another conformation by introducing a penalty term into the objective function [56]. Distributed multipole analysis [59] provides another way to regenerate the electrostatic potential, that is essentially an extended and modified population analysis in the sense that it has the higher moments of overlap distribution included in the multipole analysis between two basis functions in addition to the charge distribution as in Mulliken's analysis. The multipole analysis gives a set of multipole expansions with their origins located at the 'centers of the overlap distributions' defined in the paper by Stone [59]. Those expansions are then transformed into the molecular-based distributed multipole expansion with point charges and/or multipole moments originated on the atoms and the 'center of bonds' also defined in the same paper. The distributed multipole analysis itself provides a convenient and straightforward way to derive the parameters of the electrostatic potential for molecular simulation. Alternatively, it can be used to regenerate the electrostatic potential of the molecule, which can then be used to derive the partial charges [60, 61].

In this work, partial charges have been fitted to the quantum mechanically generated electrostatic potential with the Boltzmann factor weighting. During the calculation of the torsional potential energy profile, electrostatic potential charges for each atom have been obtained with the Merz-Singh-Kollman [53, 62] algorithm at each different conformation. Weighted charges on each atom have then been calculated, using Boltzmann weighting factors at 300K corresponding to each conformation. These weighted charges have been used to derive a single set of explicit-atom partial charges by averaging over conformations as follows:

$$\bar{q} = \frac{\sum_i q_i \cdot \exp\left(-\frac{E_i}{kT}\right)}{\sum_i \exp\left(-\frac{E_i}{kT}\right)} \tag{5}$$

where the summation is over all the conformations. The partial charges from each atom of a given united atom group are then summed to give the united-atom partial charges for the molecule.

LJ parameters: Once the partial charges and intramolecular potentials have been obtained by the approaches described above, Gibbs ensemble Monte Carlo simulations are then used to derive the Lennard-Jones parameters. For perfluoroethers, the introduction of oxygen atoms changes the electron distribution of the neighboring CF_x sites and hence the Lennard-Jones parameters of them. Therefore, there are more parameters that need to be adjusted separately than as in perfluoroalkanes. To speed up the searching process for the optimized parameter set, an alternative to Gibbs ensemble

Monte Carlo simulation, Gibbs-Duhem integration, is applied in this work and will be discussed later.

2.1.2 Gibbs ensemble Monte Carlo simulation

In 1987, Panagiotopoulos [47] proposed a new ensemble, the Gibbs ensemble, for Monte Carlo simulation. In the Gibbs ensemble, three different types of trial configurations on two separate simulation boxes are generated; displacement of particles (translation, rotation, and molecular conformation), volume changes, and molecule exchanges which are carried out in order to achieve equilibration of the temperature, pressure, and chemical potential between the simulated coexisting phases. This new ensemble allows the direct simulation of phase equilibrium with the Monte Carlo method and has been proved to be a really powerful tool for determination of phase equilibrium properties.

Since its introduction, Gibbs ensemble Monte Carlo simulation has become an important tool and has been applied to several areas with phase coexistence. Soon after the Gibbs ensemble was proposed, it was applied to the phase equilibrium simulations of supercritical fluid mixtures [63] and ionic liquids [64]. De Pablo et al. [65] used Gibbs ensemble Monte Carlo simulation to calculate the saturated densities and enthalpy of vaporization in vapor-liquid-equilibria of several polyatomic fluids with site-site Lennard-Jones potentials.

However, the Gibbs ensemble Monte Carlo method becomes very difficult at high density and when the simulated fluid is composed of chain molecules with several

sites because of the particle exchange step. The configurational-bias Monte Carlo method based on Rosenbluth and Rosenbluth's self-avoiding random walk algorithm was proposed by Siepmann and Frenkel in 1992 [66, 67] and simultaneously by de Pablo et al. [68, 69] to enable the Gibbs ensemble to be used in such circumstances by cutting and re-growing the molecule one site at a time instead of trying to put in the whole molecule at the same time. Wick and Siepmann [70] proposed an extension of the configurational-bias Monte Carlo move that can be applied to chain molecules with strong intramolecular interactions at fixed ends, or in other words bonded ends, which excludes the application of the normal configurational-bias Monte Carlo method because an end of molecules is difficult to find in such system. This new move allows the molecule to be cut in the middle and hence is applicable to cases such as networks, high molecular weight polymers, and cyclic molecules.

Another problem with Gibbs ensemble Monte Carlo simulation is that, because of the finite size effect, the Gibbs ensemble Monte Carlo simulation becomes unstable in the near-critical region. The finite size effect of the Gibbs ensemble Monte Carlo simulation has been studied by Moon and Binder [71], Recht and Panagiotopoulos [72], Wilding [73], and Bruce [74]. Valleau [75] showed that Gibbs ensemble Monte Carlo could be performed in the near-critical region only if the total volume is carefully adjusted so that the number of particles in both boxes is equal. However, it is not required for simulations well outside of the critical region.

Harris and Yung [30] proposed a potential model for carbon dioxide, the EPM model, with point charges and Lennard Jones interactions. The EPM model closely

predicted the coexistence curve and critical properties compared to experimental values. Siepmann et al. [76] studied the phase behavior and reported the phase diagrams of linear hydrocarbons up to C_{48}. Later, Smit et al. [77] developed a united atom potential model for n-alkanes which closely reproduced their phase envelopes. The critical properties of long chain n-alkanes, for which contradictory results had been reported from different experiments, are also obtained and the trend that the critical densities decrease with increasing chain length for C_8-C_{48} is also verified. This potential model was later extended to branched alkanes [78]. VanLeeuwen [79] derived the potential model parameters of alkanols by combining the parameter sets for alkanes and methanol using Gibbs ensemble Monte Carlo simulation. Cui et al. [80] performed Gibbs ensemble Monte Carlo simulations with Smit's [77] model on several n-alkanes and their branched isomers. The results were in reasonable agreement with the experiments. Mackie et al. [81] applied the same model to the mixtures of methane/n-dodecane and methane/n-pentane. Cui and Siepmann et al. [82] proposed two sets of potential parameters for perfluoroalkanes that generated the critical temperature and saturated liquid densities in good agreement with experimental data. Cui's model [83] was latter used to study the solubility difference between alkanes and perfluoroalkanes in CO_2, and concluded that the dispersion interaction and the geometric packing may be the major factors. The transferable potentials for phase equilibria with united atoms, TraPPE-UA, for normal and branched alkanes, alkenes, and alkylbenzenes [84-86], and with explicit hydrogens, TraPPE-EH, for normal alkanes [87] were later developed by Siepmann's group using Gibbs ensemble Monte Carlo simulation for phase equilibrium

calculations. Errington and Panagiotopoulos [88] proposed a model with a Buckingham exponential-6 potential for the homologous series of n-alkanes, which showed good agreement with experimental data in critical densities and temperatures. The model is comparable to previous models in saturated liquid properties but better in vapor pressure calculations.

From the examples above, it is clear that Gibbs ensemble Monte Carlo simulation has been widely used for developing potential models that are suited for condensed phase and/or phase equilibrium simulations. And the force fields so obtained can be applied to the simulation of related areas.

2.1.3 Gibbs-Duhem Integration

As described above, Gibbs ensemble Monte Carlo simulation provides a direct and practical means for studying the phase equilibrium properties. However, the particle exchange move in the Gibbs ensemble Monte Carlo simulation involves the particle insertion which becomes difficult or even impossible for systems composed of long chain molecules and/or at high densities as previously mentioned. Besides, for a coexistence line, several simulations at different state points on the line are needed, which can become very time-consuming when the process needs to be performed repeatedly, for example while optimizing the parameters of a potential model. To simplify the procedure of modeling phase coexistence, Kofke and coworkers [48, 89, 90] proposed a method based on thermodynamic integration.

In its original practice [89], the Clapeyron equation was derived from the Gibbs-Duhem equation as:

$$\left(\frac{dP}{d\beta}\right)_{eq.} = -\frac{\Delta\underline{H}}{\beta\Delta\underline{V}} \tag{6}$$

where P is pressure, β is 1/kT (k is the Boltzmann constant), $\Delta\underline{H}$ and $\Delta\underline{V}$ are the difference in molar enthalpy and molar volume of the two coexisting phases, and the subscript *eq.* at the left hand term indicates that the derivative is taken along the saturation line. The right hand side of equation (6) is a function of pressure and temperature and can be evaluated along the saturation line by either molecular dynamics or Monte Carlo simulations with an NPT (isothermal-isobaric) ensemble. Given an initial state point, equation (6) can then be integrated to give the coexistence line providing that the right hand term is evaluated for at least one point along the line.

Since its introduction, the Gibbs-Duhem integration method has been applied and extended to multiple-phase equilibria [91], solid-liquid equilibria [92, 93], and chain molecules [94, 95]. One of the important extensions is in studying the effect of varying the potential model upon the coexistence line [96-98]. Agrawal and Kofke [96] studied solid and liquid coexistence of particles with a soft sphere potential:

$$u(r,n) = \varepsilon\left(\frac{\sigma}{r}\right)^n \tag{7}$$

where r is the intermolecular distance, ε and σ are the energy and size parameter, and n is the hardness parameter. The solid-fluid transition pressures for systems with different n were investigated with Gibbs-Duhem integration. Sturgeon and Laird [98] derived the

parameters for an embedded atom model of aluminum by adjusting the melting temperature to the experimental value while not significantly affecting the other mechanical properties with Gibbs-Duhem integration. This application showed that in addition to the numerous extensions suggested and reviewed by Kofke [97], Gibbs-Duhem integration could be used to locate an optimized set of potential parameters. For a thorough review on the Gibbs-Duhem integration, the review article by Kofke [97] is the most recent article that covers the fundamentals (derivation of the equations) and applications. Our implementation and application of the Gibbs-Duhem integration method for determining the Lennard-Jones parameters of perfluoroethers is presented in appendix B.

CHAPTER 3

RESULTS AND DISCUSSION

In this work, a potential model for perfluoroethers has been developed based on the intramolecular force field obtained from *ab initio* calculations, and the Lennard Jones parameters obtained with Gibbs ensemble Monte Carlo simulation and Gibbs-Duhem integration technique. The first part of this work, which developed a preliminary potential model for perfluoromethylpropylether along with the *ab initio* calculation results for the same molecule has been accepted for publication. To extend and generalize the potential model, *ab initio* calculations for the other modeled molecules were carried out. The results show some interesting behavior of the modeled molecules, which are discussed in detail later in this chapter. The application of Gibbs-Duhem integration technique to potential model development, as adapted for this work, and its potential in automating the parameterizing process are also demonstrated. And finally, the generalized potential model is shown to reproduce the phase envelope and critical properties of the modeled molecules correctly.

3.1 Results of *ab-initio* calculations

Because of the limited experimental data, only three perfluoroethers with available phase equilibrium data have been used in the potential model development. The molecules are perfluoroethylmethylether (CF_3-O-CF_2-CF_3), perfluoromethylpropylether (CF_3-O-CF_2-CF_2-CF_3), and perfluorodimethoxymethane (CF_3-O-CF_2-O-CF_3) as shown in figure 1. As previously mentioned, a united atom representation of the molecules has been applied in this work because of its simplicity and its efficiency in simulations. In figure 2, CF_3-O-CF_2-CF_2-CF_3 is used as an example to explain the grouping for united atoms in this work and the definition of some simplifying symbols that will be used later.

To obtain the intramolecular terms of the potential model and the partial charges for the electrostatic potential, electronic structure calculations, described in subsection 2.1.1, were carried out with Gaussian 98®. In the following sub-sections, the results of the *ab initio* calculations will be shown and discussed, including the bonded terms of the potential model such as the bond lengths, bond angles, and the torsional potential, as well as the partial charges for the non-bonded electrostatic potential.

3.1.1 Geometry optimization

The optimized geometries of the perfluoro-compounds such as perfluoroalkanes and perfluoroethers are usually quite different from those of their hydrogenated counterparts because of the replacement of the small hydrogen atoms by the bulky fluorine atoms. The structures of perfluoroethers are further complicated by the fact that

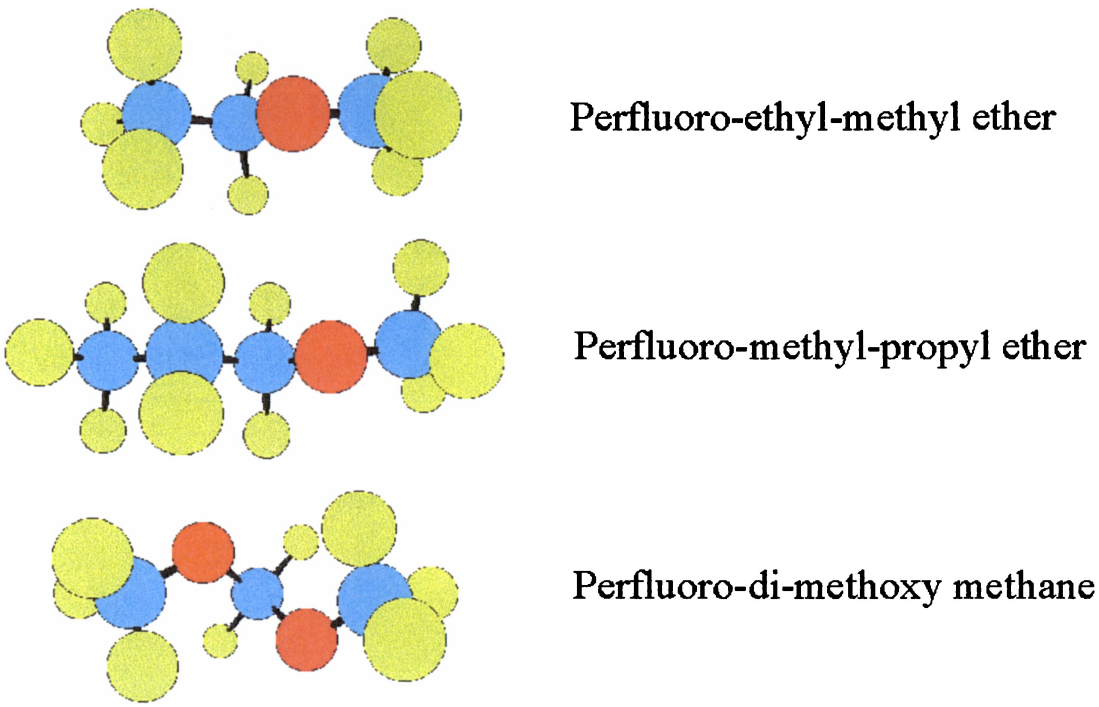


Figure 1. Diagrams of the modeled molecules, perfluoroethylmethylether, perfluoromethylpropylether, and perfluorodimethoxymethane.

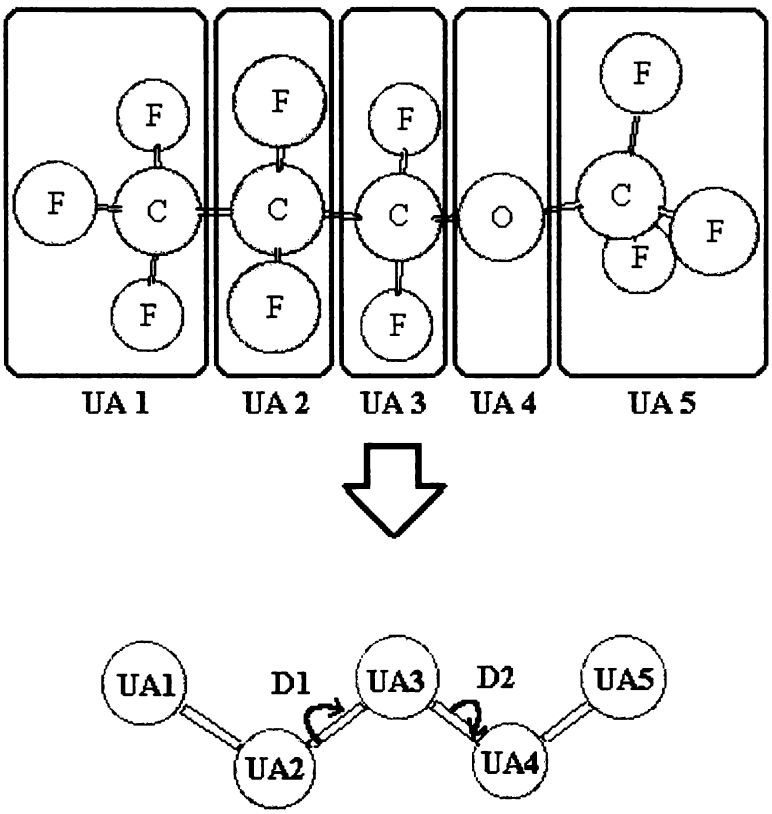


Figure 2. Schematic of the grouping of the united atom, and the assigning of the two dihedral angles.

the O-C bond length, ~1.36 Å, is shorter than that of the C-C bond length, ~1.536 Å. In the rest of this subsection, diagrams of each simulated molecule will be shown and be used to demonstrate the optimized structure. It has been shown that [99] the results of geometry optimization from self-consistent methods such as restricted Hartree Fock with 6-31G* basis set are generally reasonably accurate. For example, the errors are generally smaller than 0.03 Å in bond length and smaller than 2^{o} in bond angle. This level of accuracy is more than enough for the proposed potential model; therefore, no further tests against experimental data were conducted.

Figure 3 shows the optimized geometry and the schematic representations from different perspectives for perfluoroethylmethylether. In this figure, the green, gray, and red balls or sticks represent the fluorine, carbon, and oxygen atoms, respectively. And the pink balls and sticks correspond to the electron lone pair on oxygen. Figure 3a is a ball-and-cylindrical-bond diagram, and the sizes of the balls correspond to forty percent of the van der Waals radii of the atoms. The reduction in the size is to avoid blocking of some atoms in the diagram. With full-scale van der Waals radii, the carbon atoms are mostly buried by fluorine atoms. In figure 3b, C1, C2, and O3 are on the same plane and the sight path is from C1 through C2. The three green sticks with spots on the tips belong to C1, and the other two sticks out of the same center, C, belong to C2. It is worthwhile to point out that the six sticks from center C almost equally dissect a circle of 360 degrees just as is normally seen in the hydrogenated alkanes. In figure 3c, C2, O3, and C4 are on the same plane with sight path going from O3 through C2. From the figure, it is clear that the optimized dihedral angle C1-C2-O3-C4 for

perfluoroethylmethylether is not 180° because of the size of fluorine atoms, and the calculated value is –162.48°. For the purpose of comparison, the optimized dihedral angle of perfluoro-normal-butane with same level of theory and basis set is –165.90°. In figures 3d and 3e, atoms C2, O3, and C4 are on the same plane as in figure 3c. The sight paths are from C4 through O3 and from C4 through C2 for 3d and 3e, respectively. In figure 3e, the three sticks with spots on their tips belong to C4 and the other 2 from the same center belong to C2. Comparing figure 3d and 3b, the fluorine atoms on C4 are slightly rotated to avoid direct eclipse with the two fluorine atoms on C2. From figure 3e, it is seen that the distortion of the dihedral angle also helps the fluorine atoms on C2 and C4 get as far away from eclipse position as possible. If C1 were on the same plane as the others, the two fluorine atoms on C2 would be pushed closer to the eclipsed position with those on C4. This seems to suggest that the distortion of the dihedral angle is caused by the fluorine atoms on carbon centers C2 and C4 rather than those on centers C1 and C4, as one might think. To further clarify whether this is the case, the optimized structure of perfluoro-normal-butane is compared with that of perfluoroethylmethylether as shown in figure 4.

In figure 4a, atoms C1, C2, and C3 are on the same plane, and the three sticks with spots on their tips belong to C1. Figures 4b and 4c are exactly the same as figures 3b and 3d. Comparing figures 4a and 4b, the difference between these two is that the third center on the backbone in 4a is carbon while that on 4b is oxygen. There are three major effects from this change; the removal of the bulky fluorine atoms, the

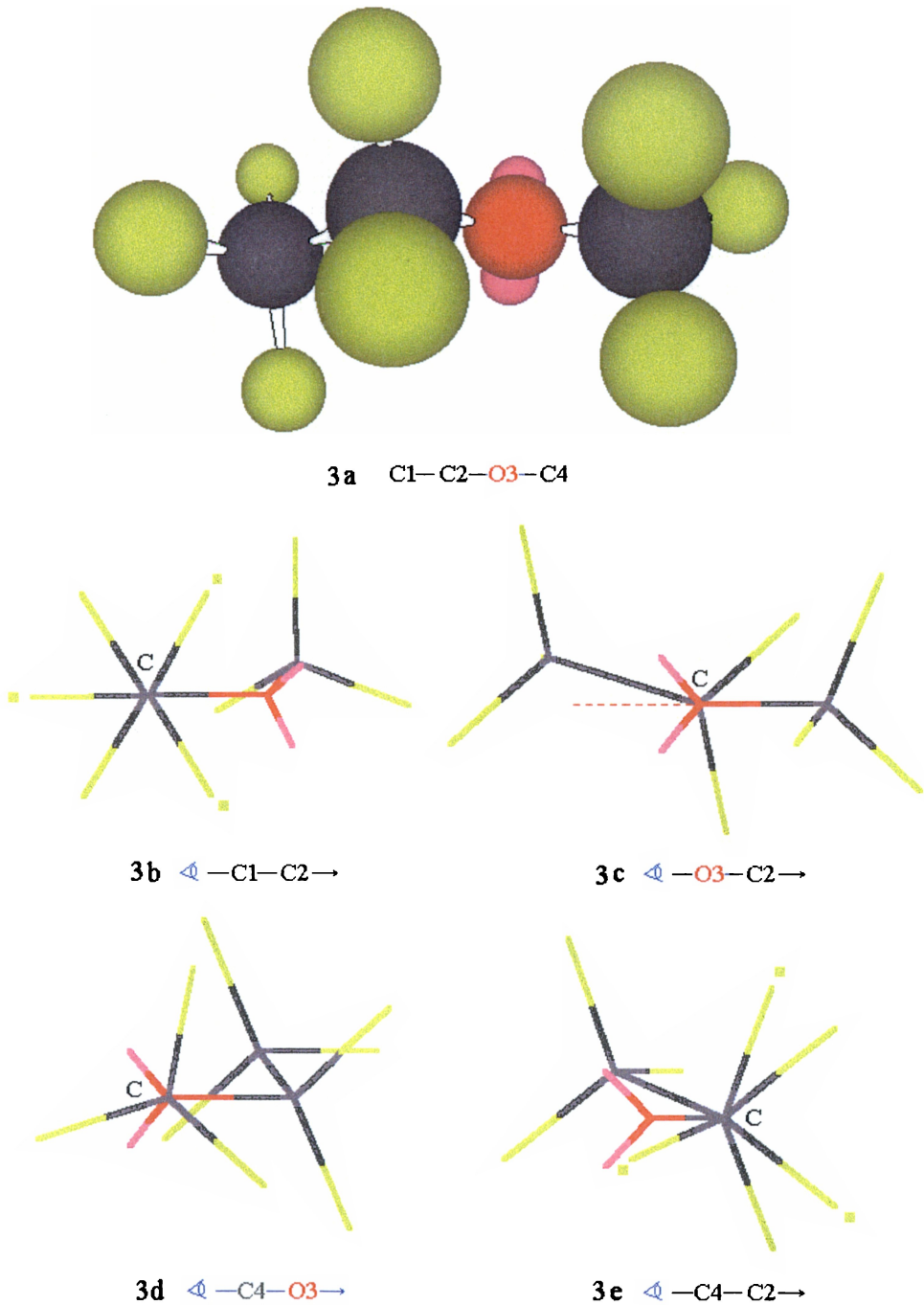


Figure 3. Diagram of the optimized structure of perfluoroethylmethylether and schematic representations of the structure.

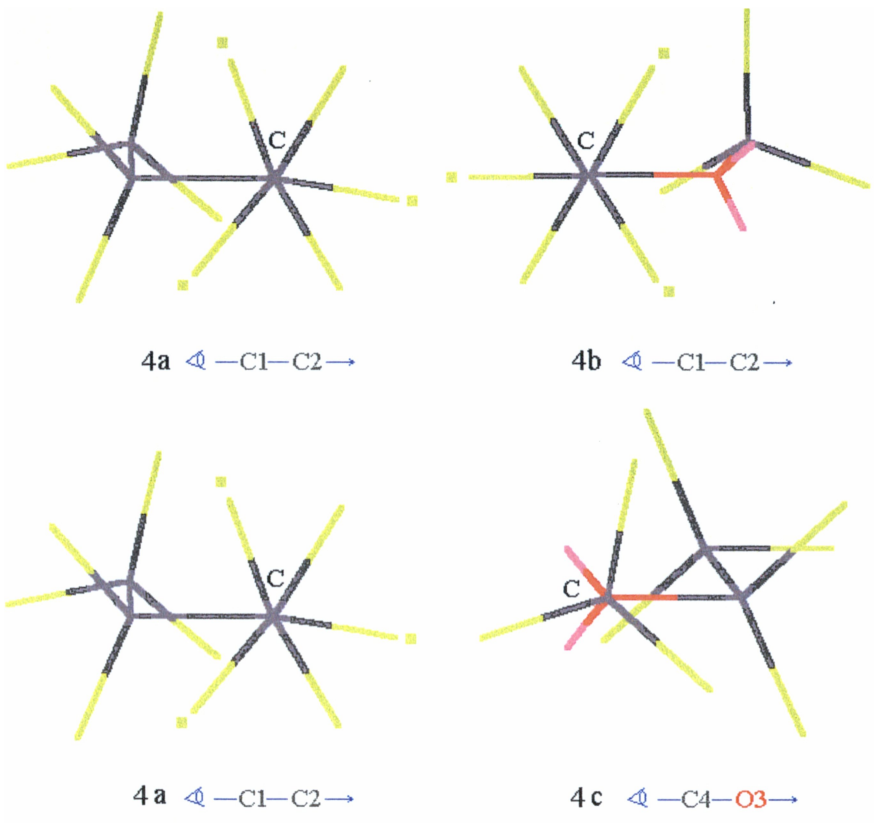


Figure 4. Comparison of optimized structures of perfluoroethylmethylether and perfluoro-normal-butane.

shortening of bond lengths, and the widening of the bond angles. In figure 4b, the fluorine atoms on C1 almost equally dissect the 360 degrees as previously mentioned, but in figure 4a they are slightly rotated away from that configuration. The longer bonds on perfluoro-normal-butane should reduce the interactions between atoms and hence allow the structure to be more like normal butane, but this is not the case as is seen here. Therefore, one conclusion that can be drawn from this comparison is that the fluorine atoms on center C3 cause the rotation. Additional proof can be provided by the comparison of figure 4b and figure 4c. It is obvious from the perfect dissection in figure 4b that the fluorine atoms on C4 do not have such strong interaction with those on C1 as to cause the rotation seen in 4a or 4c. The only reason left that can explain the rotation is the fluorine atoms on C2. Following the arguments above, it is concluded that the rotation away from the perfect dissection is due to the repulsion between fluorine atoms on C2 and C4. However, because of the electron lone pairs on O3, the rotation is limited. Therefore, the optimized dihedral angle is distorted to further alleviate the repulsion. This reasoning can be confirmed by examining the structure of CF_3-O-CF_2-O-CF_3.

In figure 4, 4a is also copied next to 4c to show that fluorine atoms on C4 of perfluoroethylmethylether are further away from the perfect dissection positions, which is, without a doubt, due to the shorter C-O bond length. The same reason is also responsible for a larger distortion in the optimized dihedral angle of perfluoroethylmethylether, 17.52°, compared to that of perfluoro-normal-butane, 14.10°.

Figure 5 shows the optimized structure of perfluoromethylpropylether. There are two types of dihedral angle in this molecule, C-C-C-O and C-C-O-C. In figures 5b and 5c, atoms C1, C2, and C3 are set on the same plane with sight paths going from C2 through C3 and C1 through C2, respectively. In figure 5b, O4 is located almost on the same plane of C1-C2-C3, which means the optimized angle for this particular dihedral angle is almost 180^{o} (177.35^{o} to be exact). In this case, the shortening of the bond length is not so significant because only one bond length is shortened instead of two as in the case of dihedral angle, C-C-O-C, and the removal of the bulky fluorine atoms reduces the steric hindrance to allow the molecule to be more flexible along this dihedral angle. Figure 5c further confirms this explanation.

On the other hand, the C-C-O-C dihedral angle in this molecule is much more like the same dihedral angle in a shorter perfluoroethylmethylether. Figures 5d and 5e are equivalent to figures 3d and 3e in terms of perspective and terminology except for the addition of an extra CF_2 on the far side of the oxygen. By comparing figure 5d to 3d and figure 5e to 3e, it is clear that the structure of this dihedral angle is, indeed, very similar to that in perfluoroethylmethylether at the optimized position. Later in this section, it is shown that these two dihedral angles also have similar energy profiles along the rotation of each angle, suggesting that the atoms related to those two angles adjust similarly to the rotation, and hence allow them to share same torsional potential (the transferability of the bonded terms of the potential model).

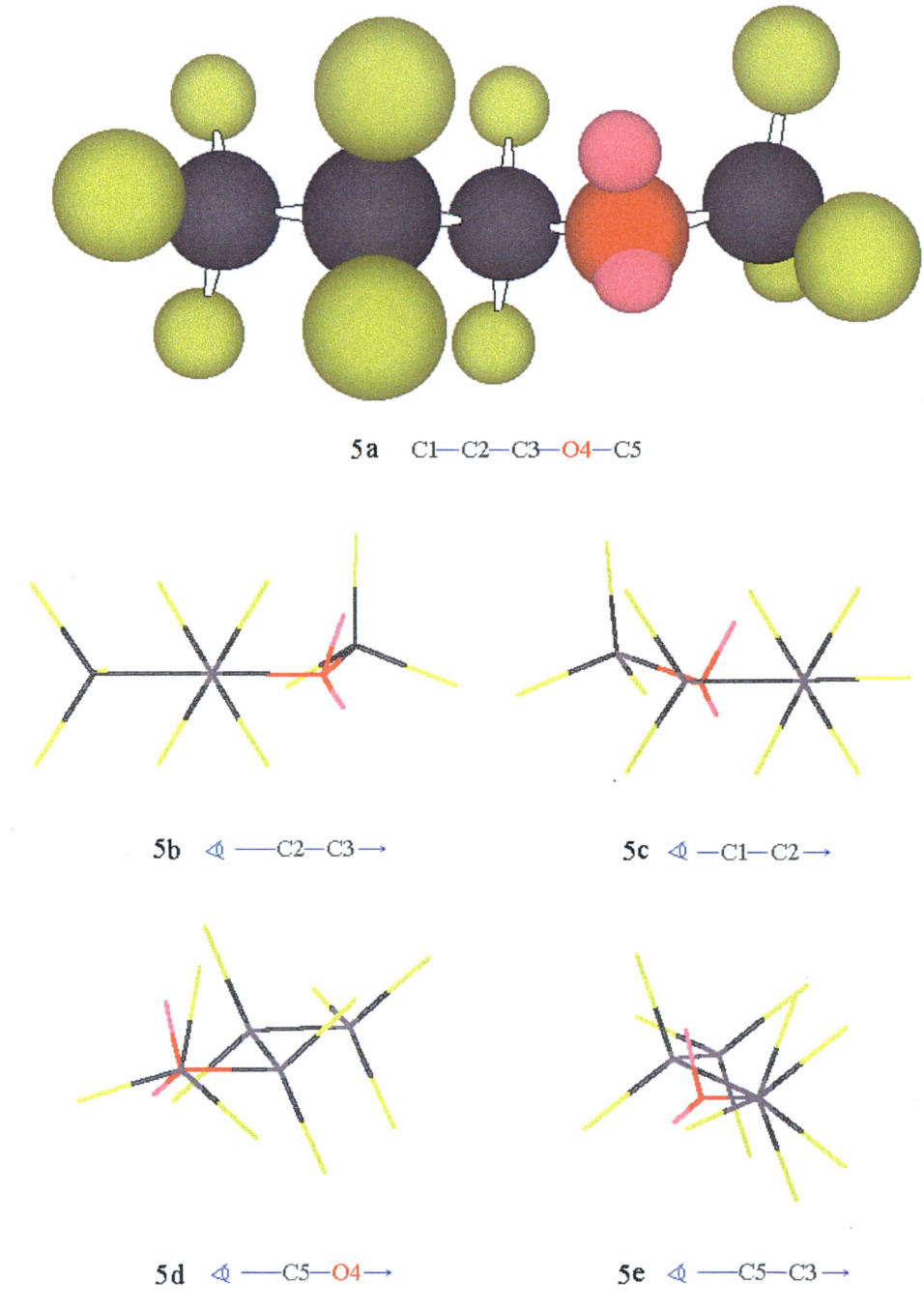


Figure 5. Diagram of the optimized structure of perfluoromethylpropylether and schematic representations of the structure.

The effects of shortened bond lengths can be seen most obviously in the molecule of perfluorodimethoxymethane, which has four shorter C-O bonds because of the introduction of two oxygen atoms. In figure 6a, the molecule is seen to be highly distorted. The optimized structure has two C-O-C-O dihedral angles at 46.72° and –163.31° respectively. This further confirms that the structural distortion at the optimized position is not solely due to the 1-4 interactions on the backbone but rather more to the interactions between fluorine atoms on the 1-3 backbone sites, because both of the 1-4 backbone interactions are CF_3-O interactions and would not have effect like CF_3-CF_2 interactions.

The severe distortion in the optimized structure may seem surprising at first, but it really is logical after all. Figure 6b is a non-optimal zigzag structure of the molecule. From the figure, one can see that if one of the CF_3 end groups is to rotate to the other side as in the optimized structure, those fluorine atoms on the three CF_x sites could be further apart and hence reduce the repulsion. Figures 6c, 6d, and 6e are from perspectives similar to figure 5c, 5d, and 5e. Comparing 5c and 6c, it is seen that the fluorine atoms on C3 can no longer align to those on C1 because of the shorter distance. This rotation along O2-C3 bond also leads to the structure in figure 6d since the difference between 5d and 6d is actually just the position change of the C5 site and the lone pairs on O4, which is the result of the rotation. Figure 6e again shows the results of the rotation and explains why the same distortion is not seen with C-C-C-O dihedral

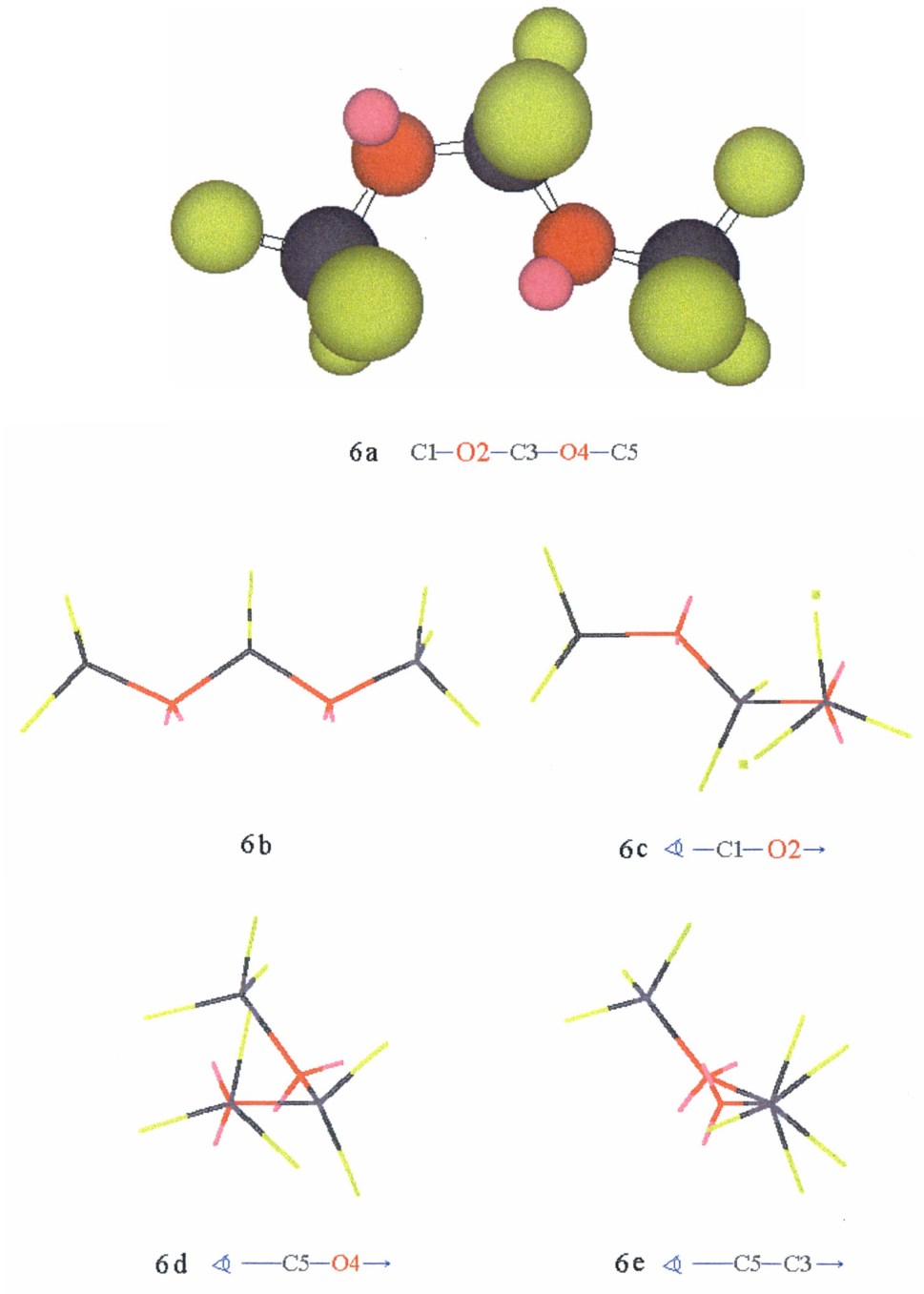


Figure 6. Diagram of the optimized structure of perfluorodimethoxymethane and schematic representations of the structure.

angle in perfluoromethylpropylether. For the same rotation to happen in perfluoromethylpropylether, the lone pairs on O2 in 6e would have to be replaced by bulky fluorine atoms which would cause significant repulsive interaction with fluorine atoms on C3. The complexity along the torsional rotation in this molecule is also seen in the energy profile later in this section.

To sum up the geometry optimization, table 1 lists the bond lengths, bond angles, and dihedral angles of the optimized structure for each molecule. In the simulation of thermophysical properties, those intramolecular terms do not have great effect on the results. Therefore, a generalized set of parameters for bond lengths and bond angles has been adopted in this model. Also, the energy profile for each type of dihedral angle and its corresponding torsional potential will be discussed in next subsection. Again, it has been shown [99] that the optimized geometries for common molecules can be obtained with reasonable accuracy by *ab initio* restricted Hartree Fock calculation, and hence the results shown in this section were not compared with experimental data.

3.1.2 Dihedral energy profile and torsional potential

Unlike the rest of the intramolecular motions, torsional motion has a lower frequency; therefore, the torsional potential terms are considerably more important than bond stretching and bending terms for the intended simulations. And because the constraint energy on the dihedral rotation is much smaller than those on the bond stretching and bond bending, the rotation is not localized and hence cannot be simulated

Table 1. Optimized geometry parameters.

Molecule*	PFEME	PFMPE	PFDMM
Bond lengths (Å)			
C-C	1.529	1.536	
C-O	1.360	1.359	1.358
Bond angles (°)			
C-C-O	107.61	106.72	
C-O-C	121.40	121.39	121.79
C-C-C		115.47	
O-C-O			109.66
Dihedral Angles** (°)			
C-C-O-C	-162.48	-161.97	
C-C-C-O		-177.35	
C-O-C-O 1***			46.72
C-O-C-O 2***			-163.31

* Abbreviations:
PFEME: perfluoroethylmethylether
PFMPE: perfluoromethylpropylether
PFDMM: perfluorodimethoxymethane

** The 0 ° angle is designed at the position where the 1-4 sites eclipse each other.

*** The two C-O-C-O dihedral angles have different values at the optimized structure as mentioned in the text.

as motions around a center position as generally done in stretching and bending. To simulate the torsional motions, the relative energy of the molecule at any position along the rotation of a particular dihedral angle, the energy profile, is needed. Following the approach in section 2.1.1, the energy profile for each dihedral angle in every molecule has been generated, and the torsional potentials for each torsional rotation motion have then been obtained by fitting a particular function to the energy profile.

For perfluoromethylpropylether, there are two different dihedral angles involved, C-C-C-O and C-C-O-C. Figure 7 shows the energy profile obtained from both RHF and MP2 methods and the torsional potential fitted to the MP2 results for dihedral angle C-C-C-O in perfluoromethylpropylether. As can been seen from the figure, the energy profile is very similar to that of a simple hydrogenated alkane because of the removal of the bulky fluorine atoms and the longer C-C bond length to C-O bond length. When the dihedral angle is close to 0^{o}, the interaction between 1,4 backbone sites is significant, and the simplicity of the O site allows the dihedral angle to rotate without energy penalty. On the other hand, when the dihedral angle approaches 180^{o}, the 1-3 interaction between CF_3 and CF_2 is more significant, and the two longer C-C bond lengths reduce the repulsion between the fluorine atoms on C1 and C3. This generates an undistorted profile, as opposed to that of the C-O-C-O dihedral angle, which will be shown later. The energy profile also shows that the energy minimum is located at the 60^{o} position instead of 180^{o}. The fitted torsional potential (solid line) reproduces the energy profile almost exactly.

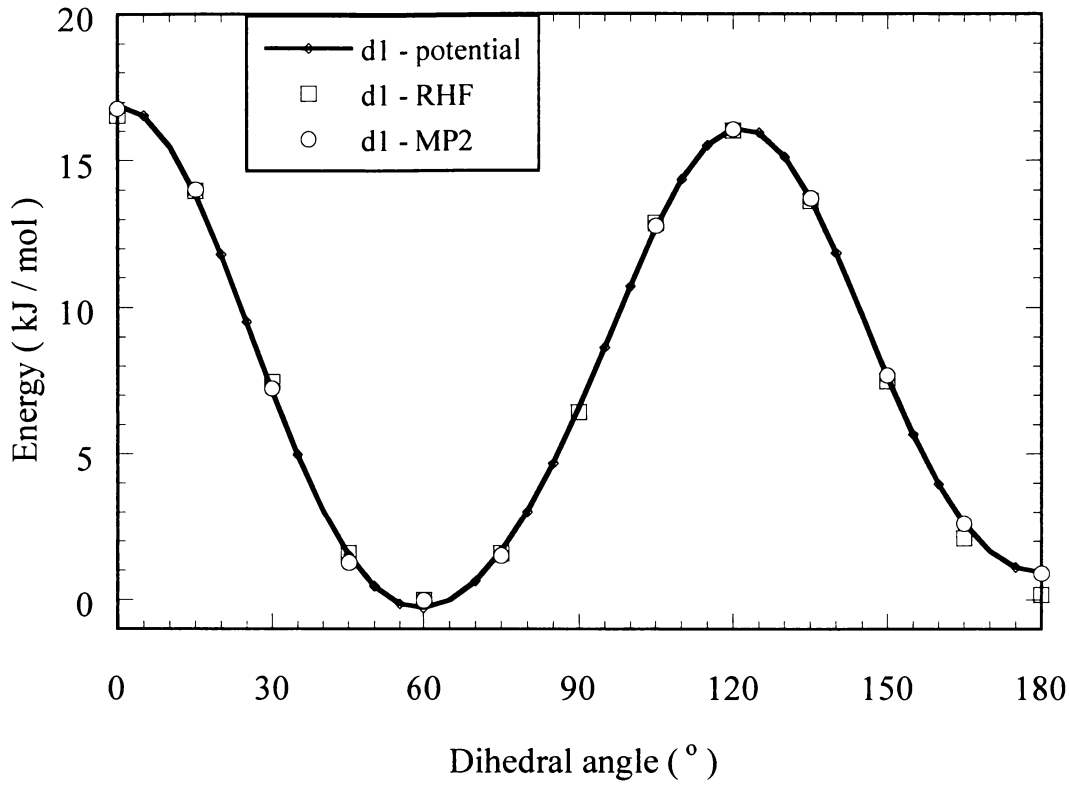


Figure 7. Energy profile and torsional potential model for dihedral angle, C-C-C-O in perfluoroethylmethylether.

Figure 8a shows the energy profile obtained from both RHF and MP2 methods and the torsional potential fitted to the MP2 results for dihedral angle C-C-O-C in perfluoromethylpropylether. The energy profile is highly distorted and is very different from that of the C-C-C-O dihedral angle; therefore, figures 8b – 8e have been added to demonstrate the cause of the distortion. In figures 8b – 8e, sites C2, C3, and O4 are on the same plane, and the sight path is from O4 through C3. The dihedral angle C2-C3-O4-C5 is at 180°, 120°, 60°, and 0° respectively. At the 180° conformation, as seen in figure 8b, the molecule is symmetrical; however, the fluorine atoms on C3 and C5 directly eclipse each other; hence, the energy is slightly higher than in the optimized conformation. In figure 8c, the molecule is still symmetrical except that the dihedral angle is at 120°, which indicates that the repulsion between C2 and C5 does not yet play an important role. As the rotation goes beyond 120°, the distance between C2 and C5 decreases, and the repulsion grows rapidly. Therefore, the energy barrier goes up instead of down as in hydrogenated alkanes or the C-C-C-O dihedral angle. The energy barrier goes through a maximum and reaches a local minimum at 60°. In figure 8d, the symmetry of C1-C2-C3 has been broken to accommodate the approach of the C5 group. Upon further rotation, the approach of the two CF_x groups, C2 and C5, begins to dominate the energy profile and leads to a dramatic increase in the energy barrier which reaches its maximum at 0° at a value almost 5 times as large as that at 120°, supposedly another maximum as in hydrogenated alkanes. In figure 8a, the fitted torsional

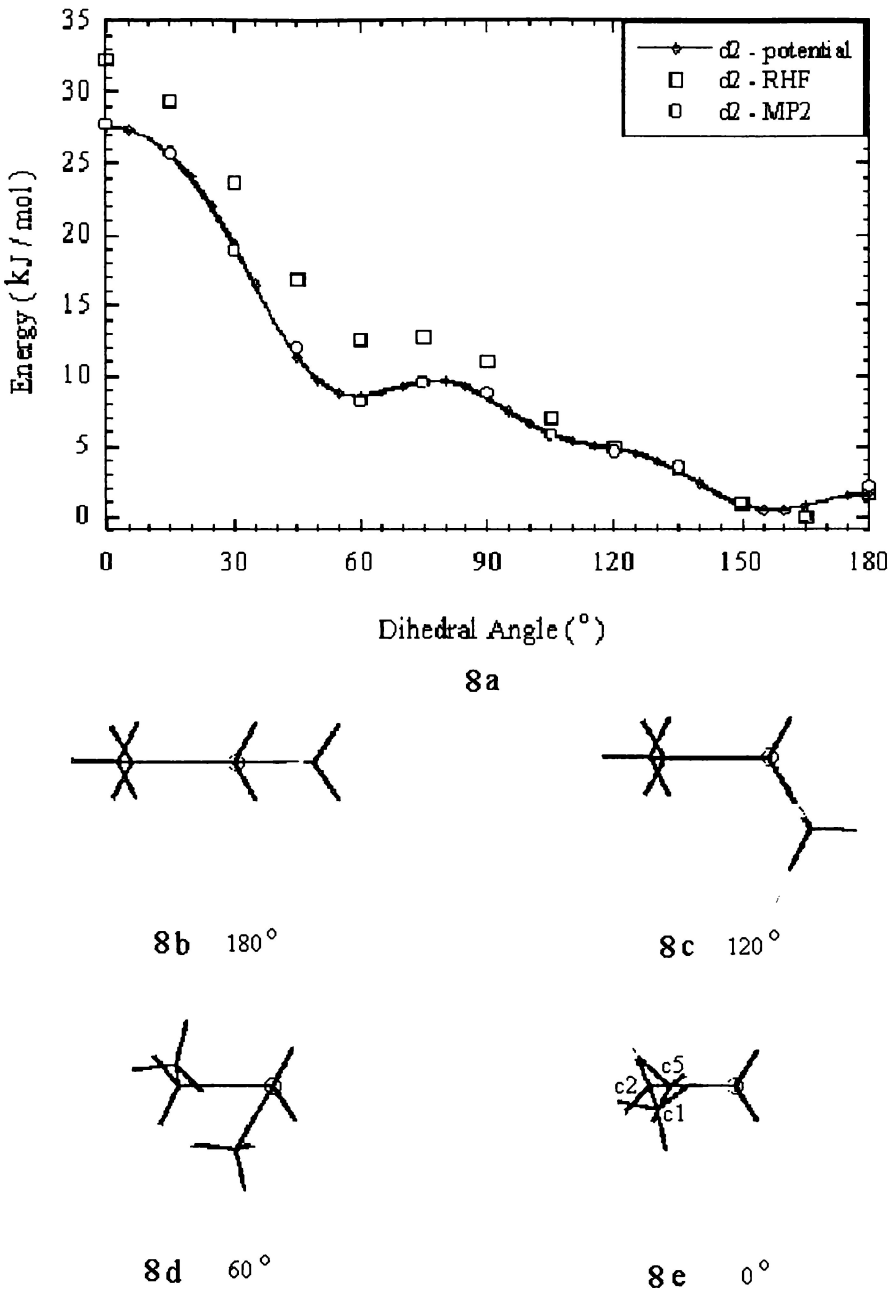


Figure 8. Energy profile, torsional potential model, and schematic representations for dihedral angle, C-C-C-O in perfluoromethylpropylether.

potential again almost exactly reproduces the energy profile, and the energy from RHF method is generally higher than that from MP2 method unlike the profiles in C-C-C-O dihedral angle. As previously mentioned, the geometries obtained with restricted Hartree Fock method are generally accurate; however, it not the case for the conformational energy [99]. Therefore, it is common practice to obtain the optimized geometry from RHF method and the energy from a higher level of method such as MP2, which is also the approach adopted in this work.

Perfluoroethylmethylether is represented by only four interaction sites in the potential model. Therefore, there is only one type of dihedral angle, C-C-O-C. The same dihedral angle also shows up in perfluoromethylpropylether. It is very important for the torsional potential of a particular dihedral angle to be the same no matter which molecule it appears in (it must be 'transferable') or the potential model will not be reliable when extended to larger molecules. To verify that the torsional potential for C-C-O-C is transferable, the energy profile along the dihedral rotation of perfluoroethylmethylether has been generated with the RHF method, and the result is compared to that of perfluoromethylpropylether with the same method in figure 9. The two energy profiles closely resemble each other. Therefore, the torsional potential for dihedral angle C-C-O-C in perfluoroethylmethylether has been adopted from that for the same dihedral angle in perfluoromethylpropylether and has not been generated separately.

Figure 10a shows the energy profile obtained from both the RHF and MP2

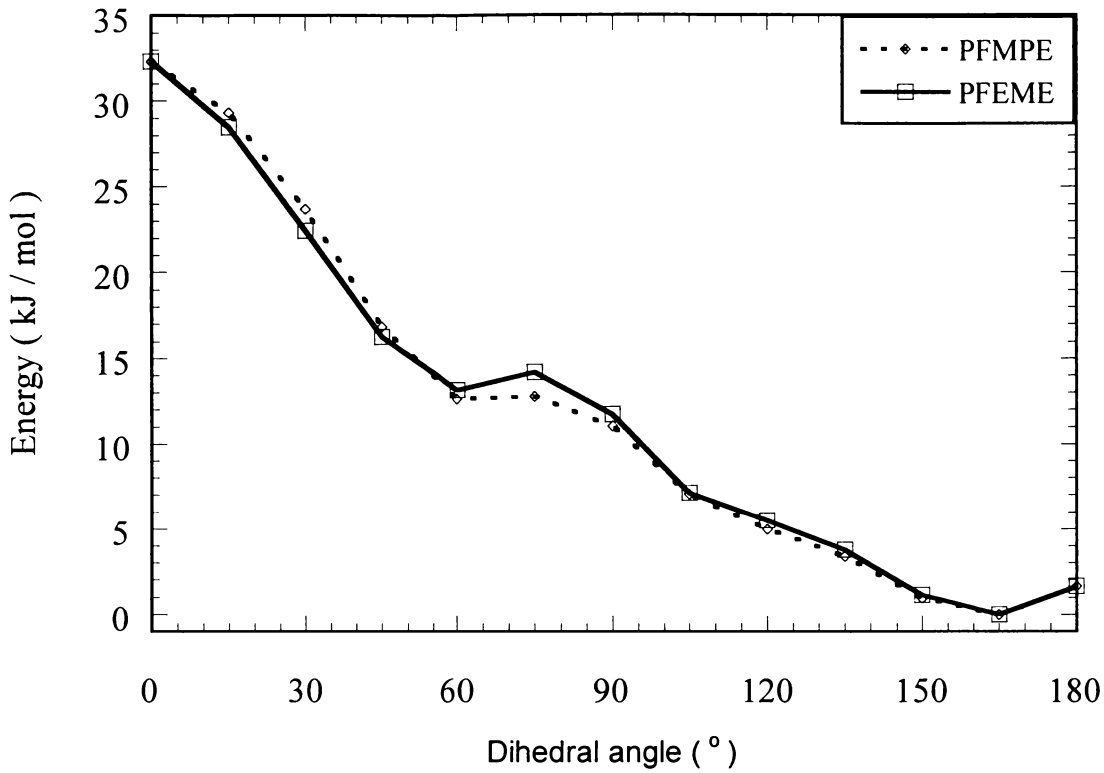


Figure 9. Comparison of the energy profiles of dihedral angle C-C-O-C in perfluoromethylpropylether and perfluoroethylmethylether.

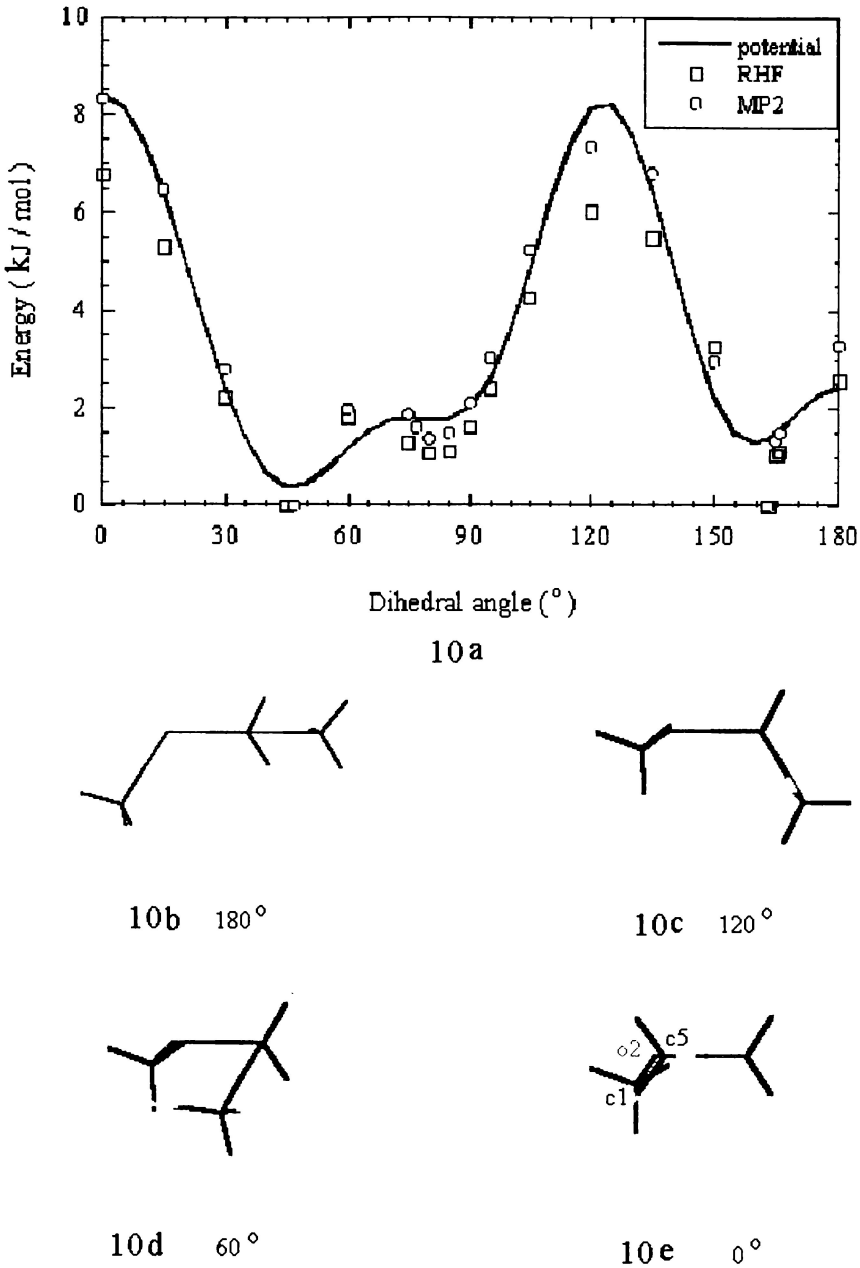


Figure 10. Energy profile, torsional potential model and schematic representations for dihedral angle, C-C-C-O in perfluorodimethoxymethane.

methods and the torsional potential fitted to the MP2 results for dihedral angle C-O-C-O in perfluorodimethoxymethane. Figures 10b – 10e are the schematic representation of rotation around this dihedral angle. In figures 10b – 10e, site O2, C3, and O4 are on the same plane, and the sight path is from O4 through C3. Dihedral angle O2-C3-O4-C5 is at 180°, 120°, 60°, and 0° respectively. In figure 10b, even with dihedral angle O2-C3-O4-C5 at 180°, the C1-O2-C3 part of the molecule is not symmetrical, unlike that in perfluoromethylpropylether. This agrees with the geometry optimization where the two C-O-C-O dihedral angles are -163.31° and 46.72°, respectively. As the molecule rotates around the dihedral angle, the energy profile goes through a minimum at ~163°, which is equivalent to the optimized conformation and then reaches a maximum at 120° shown in figure 10c. As can been seen in figure 10a, the energy profile changes so rapidly around 163° that the fitted torsional potential could not reproduce the small feature at this location. It is important to point out that the direction of the rotation, from 180° to 0° or from 0° to 180°, affects the results of partial geometry optimization.

Figure 11 shows the energy profile upon rotating both from 180° to 0° and from 0° to 180°. It can be seen that when the rotation is from 180° to 0°, the energy barrier keeps increasing instead of decreasing after 120°. This does not imply the existence of two optimized conformations since the energy of one of the conformations is much higher than the other. However, this does imply the difficulty in reaching the optimized conformation when the dihedral angle is rotated in this direction during partial geometry optimization. The difficulty is caused by the shorter C-O bond

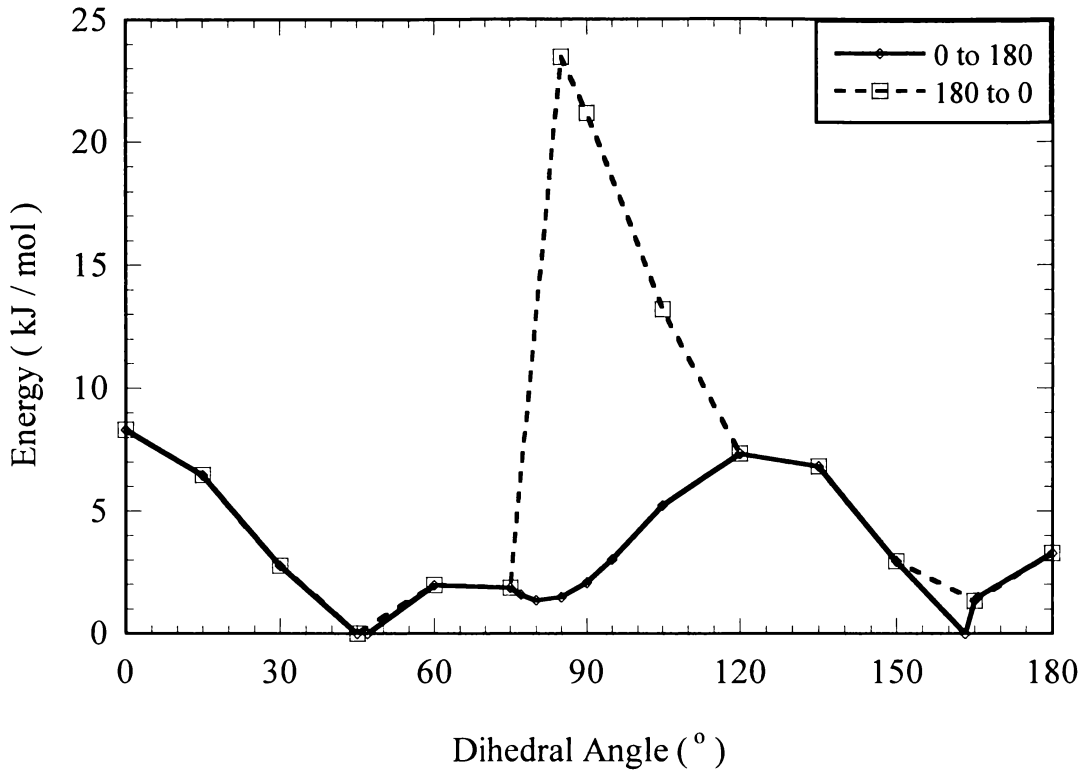


Figure 11. Comparison of the energy profiles of dihedral angle C-O-C-O in perfluorodimethoxymethane rotating in two different directions.

lengths, which hinder the molecule from adjusting to the rotation. Again, this shows the complexity of this molecule.

After passing through the maximum at 120°, the energy barrier begins to go down. However, the energy barrier does not minimize at 60° as normally seen in hydrogenated alkanes. Further rotation to ~45° allows the fluorine atoms to be further apart from each other, as explained in the previous sub-section, and hence reduces the barrier further. It is worth noting that the energy profile does not monotonically decrease from 120° to 60° but instead it goes through a local maximum at about 60°. Once the energy barrier reaches a minimum at ~45°, it begins to increase and reaches a maximum at 0 °. From figure 10a, the torsional potential does not fit the energy profile very well in this case because of the complexity of the profile. Other functional forms may give a better fit; however, for simplicity of the potential model, it is desirable to use the same functional form for all the torsional potentials. The emphasis on the complexity of the C-O-C-O torsional potential seems to suggest that the introduction of oxygen atoms does not make the dihedral angle more flexible, which is contrary to common understanding. Figure 12 shows the comparison of the three energy profiles along the corresponding dihedral angles. From the comparison, it is clear that the energy barrier in the C-O-C-O dihedral angle is indeed the lowest; hence, the introduction of more oxygen atoms does make the dihedral angle more flexible. Another interesting point that can be drawn from the comparison is that the shape of C-C-O-C and C-O-C-O energy profiles are similar between 180° and 120°, which confirms

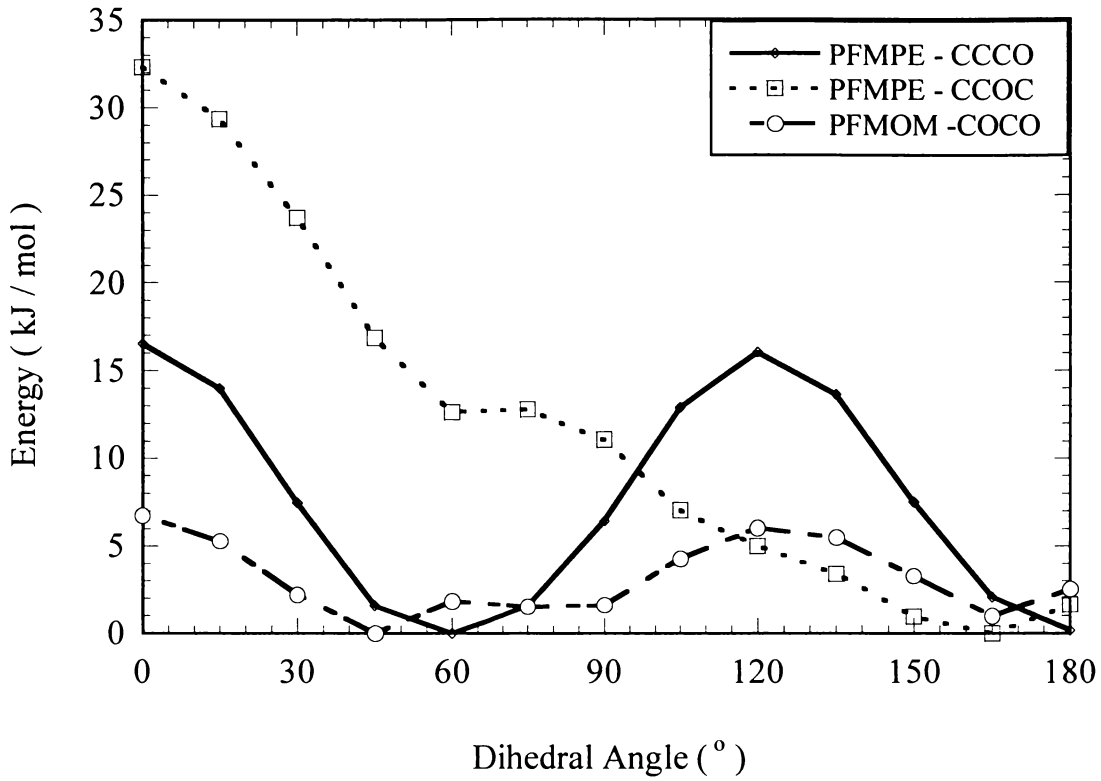


Figure 12. Comparison of the energy profiles of all three different dihedral angles.

that the distortion within this region is caused by the interaction between the fluorine atoms on the 1 and 3 carbon sites, C-O-C.

All the torsional potential models have the form of 7^{th} order polynomial of cosine(ϕ) as previously mentioned. The parameters will be listed later, along with the van der Waals parameters, as a complete set of parameters of a potential model for perfluoroethers.

3.1.3 Partial charges

The main difference between the potential models for perfluoroethers and perfluoroalkanes or between ethers and alkanes is that the oxygen atom(s) in ethers will create a shift of electron density and hence a permanent electrostatic interaction which is normally negligible in alkanes. To account for the long-range electrostatic interactions, a set of artificial point charges and/or dipoles is usually introduced into the potential model. In this work, a point charge at each simulation site has been used to represent the electrostatic interactions, and the steps described in section 2.1.1 have been followed to give a united atom partial charge set for each molecule.

Figure 13 shows the explicit atom partial charge profile upon rotation around the dihedral angle C-C-C-O in perfluoromethylpropylether calculated by RHF methods with the cc-pvdz basis set. It should be pointed out that all the partial charges in this work were obtained by the same method and basis set. The partial charges obtained with RHF and MP2 methods do not show much difference; therefore, the results from the

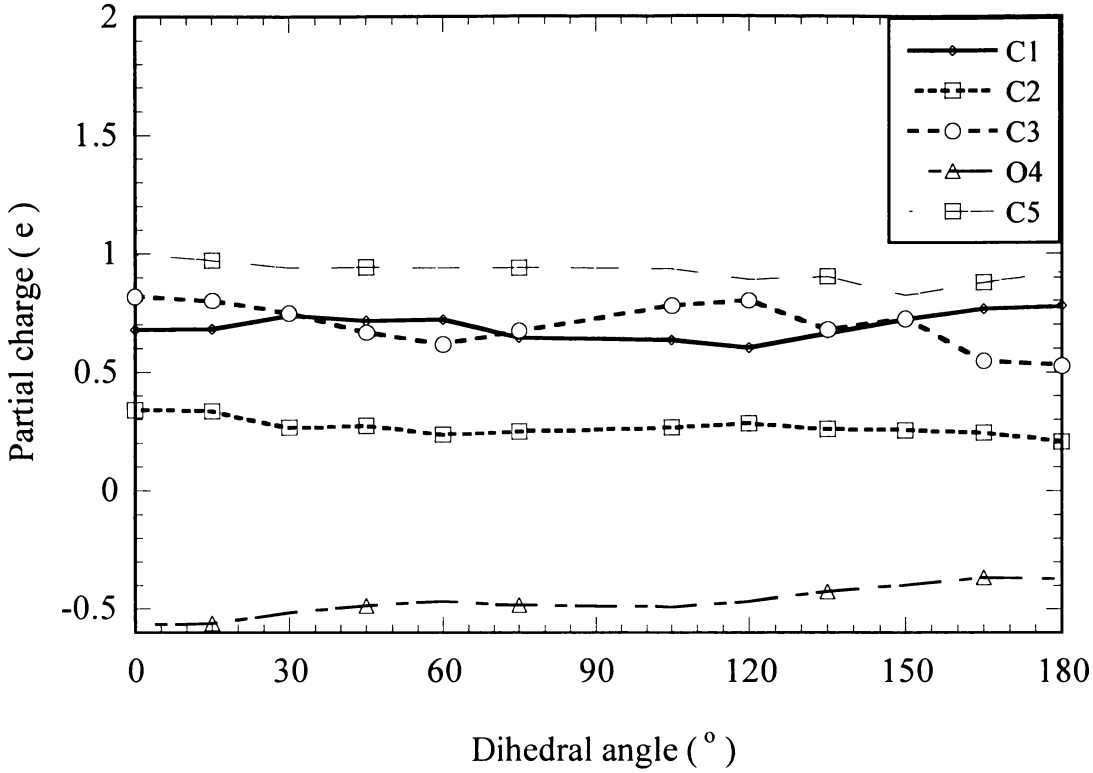


Figure 13. Explicit atom partial charge profile on rotation around dihedral angle C-C-C-O for perfluoromethylpropylether calculated by the RHF method with the cc-pvdz basis set.

RHF method have been adopted here. To simplify the picture, figure 13 shows the partial charges only on the backbone atoms. In the figure, the partial charges do depend on the conformation. However, the dependence is rather weak in this case. The five charge profiles can be roughly separated into three groups with C2 and O4 each being the single member of its respective group and C1, C3, and C5 in the third group. Not surprisingly, O4 is the only atom with negative partial charge among the five, and value of the charge is about –0.5 *e*. The positive partial charge on C2 is significantly lower than those on the third group of carbon atoms, which are close to one another, because only two electron-attracting fluorine atoms are attached to C2 and no oxygen atom. In the third group, C5 has a slightly larger partial charge than the other two because it has three fluorine atoms and is also adjacent to the oxygen.

Figure 14 is similar to figure 13 except for that the charge profiles in figure 14 are for the united atoms, which means the partial charges on the fluorine atoms have been collapsed onto the main simulation site to which they are attached. The profile for oxygen in figure 14 is the same as that in figure 13 because there are no fluorine atoms attached to the oxygen. One interesting thing to look at in the figure is the comparison of the charge profiles of UA1 and UA2, which correspond to C1 and C2 backbone sites. These two sites are separated from an oxygen atom by at least one intermediate site. The partial charges on these two sites are similar in magnitude but located at the opposite side of the zero charge line. Another interesting thing is the comparison of charge profiles for UA3 and UA5. These two sites are directly adjacent to the oxygen

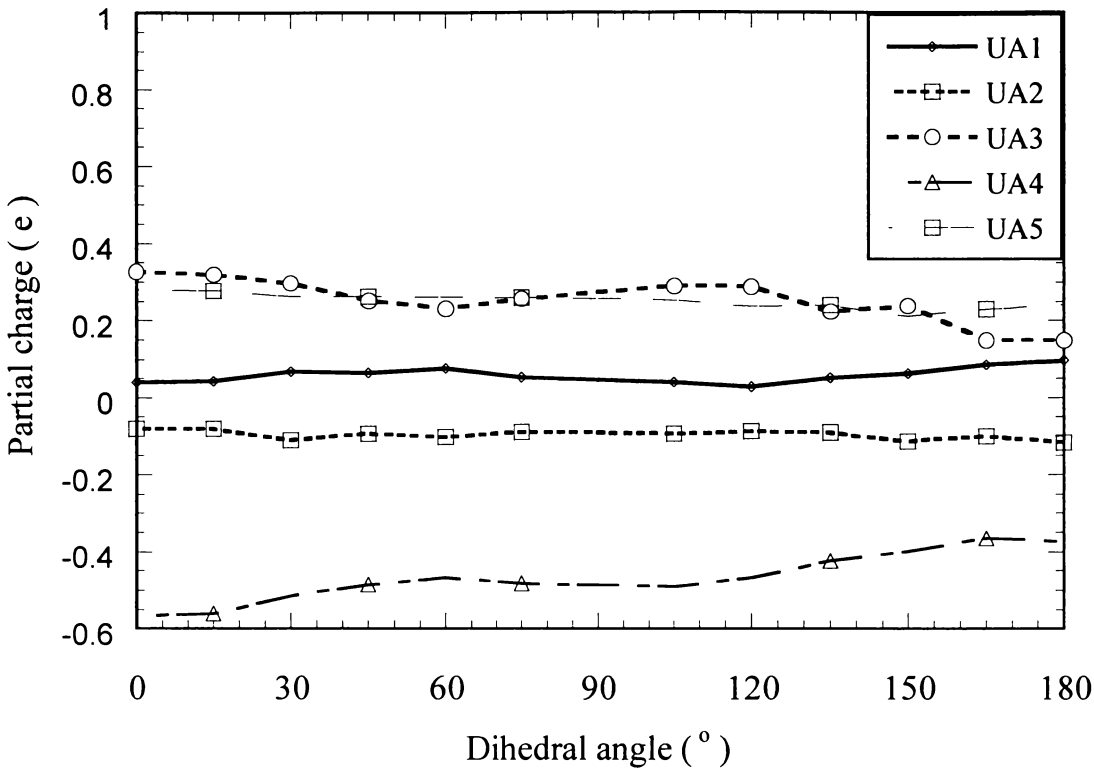


Figure 14. United atom partial charge profile along dihedral angle C-C-C-O for perfluoromethylpropylether calculated by the RHF method with the cc-pvdz basis set.

atom, and the partial charges on them are similar to each other regardless of whether it is a CF_3 site or a CF_2 site. Based on the observations above, UA1 and UA2 might be grouped in the same sub-set and UA3, UA4, and UA5 in another in the process of generalizing the partial charges for longer molecules, since the sum of a sub-set of partial charges must add up to zero. The generalization of assigned partial charges is important for modeling long-chain perfluoroethers. However, in the case of short molecules, alteration of the partial charges would have a significant effect and distort the electrostatic interactions. Therefore, it may be better to use the independently obtained partial charge set for small molecules.

The partial charges in figure 14 have been weighted by the Boltzmann factor from the energy at each conformation, and the sum of the weighted charges gives the partial charges used in this model. Figure 15 shows the profile of the weighted charges. In the figure there are two heavily weighted regions corresponding to the two minima in the energy profile, and the weighted charges outside the region are essentially zero. Figure 16 is similar to figure 15 with the dihedral angle being C-C-O-C in the same molecule instead. The observations regarding the generalized partial charges from figure 14 are still true except that the partial charge on UA3 is significantly lower than that of UA5 at the highly weighted conformation. Averaging over the profile in figures 15 and 16 from 0^o to 180^o gives the partial charges for this molecule, and the resulting weighted partial charge set for perfluoromethylpropylether is $0.08e$, $-0.11e$, $0.20e$, $-0.42e$, and $0.25e$ from UA1 to UA5.

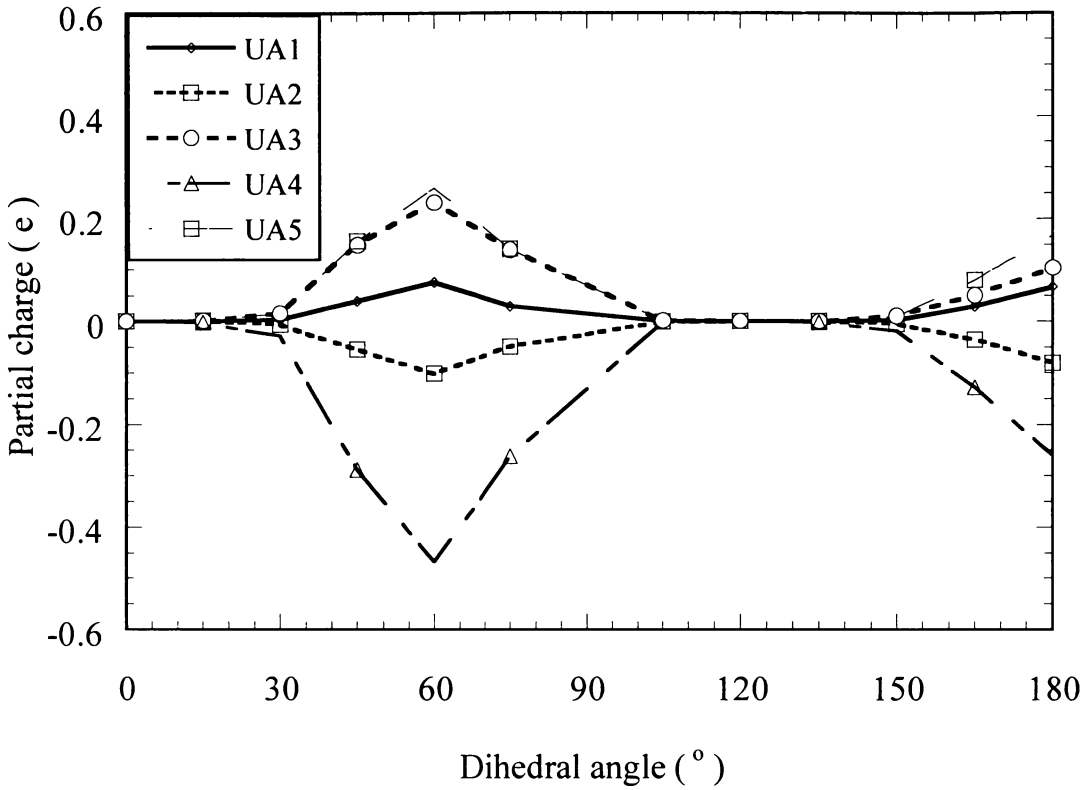


Figure 15. Weighted united atom partial charge profile along dihedral angle C-C-C-O for perfluoromethylpropylether calculated by the RHF method with the cc-pvdz basis set.

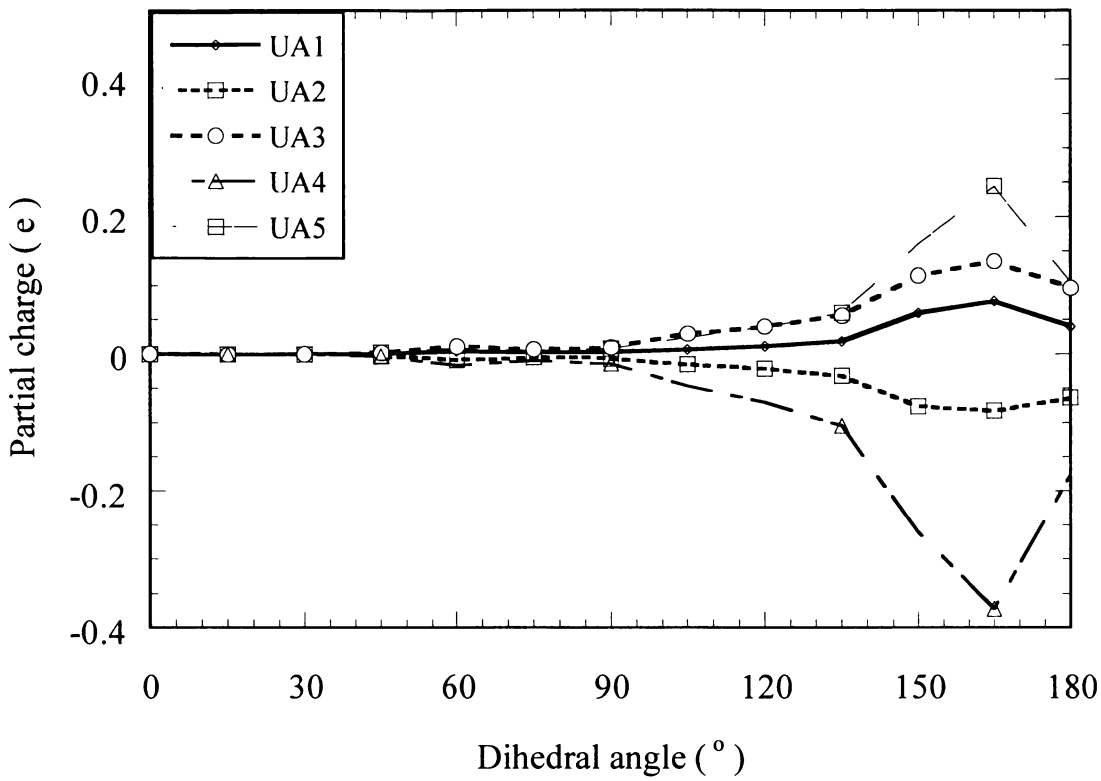


Figure 16. Weighted united atom partial charge profile along dihedral angle C-C-O-C for perfluoromethylpropylether calculated by the RHF method with the cc-pvdz basis set.

Figure 17 is the weighted charge profile along the dihedral angle C-C-O-C in perfluoroethylmethylether. The profile is similar to figure 16 because of the similar energy profile. However, in perfluoroethylmethylether, there are only four sites with UA3 being the oxygen site. The partial charge set for perfluoroethylmethylether is 0.05*e*, 0.13*e*, -0.42*e*, and 0.24*e* from UA1 to UA4. The partial charge on CF_2, UA2, in this molecule is not close to either UA2 or UA3 in perfluoromethylpropylether. This will not present a problem in generalizing the partial charges for long-chain molecules because the net partial charge on this site should include contributions from both sub-sets described above.

Figure 18 is the weighted charge profile along dihedral angle C-O-C-O in perfluorodimethoxymethane. The most obvious difference between figure 18 and the rest of the weighted charge profiles is that all the partial charges in this molecule have non-zero values throughout the span of the dihedral angle. This is because of the lower rotational energy barrier for this molecule as previously described. In this figure, the charge on UA1 and UA2 are equivalent to UA5 and UA4, respectively, because of the symmetry. The partial charge set for perfluorodimethoxymethane is 0.24*e*, 0.48*e*, 0.48*e*, -0.48*e*, and 0.24*e* from UA1 to UA5.

Because of the limited experimental data available, only three short perfluoroether molecules have been used in optimizing the potential model parameters. As previously mentioned, the alteration of partial charges, which is necessary to generate a general and transferable potential model, will cause a great distortion in

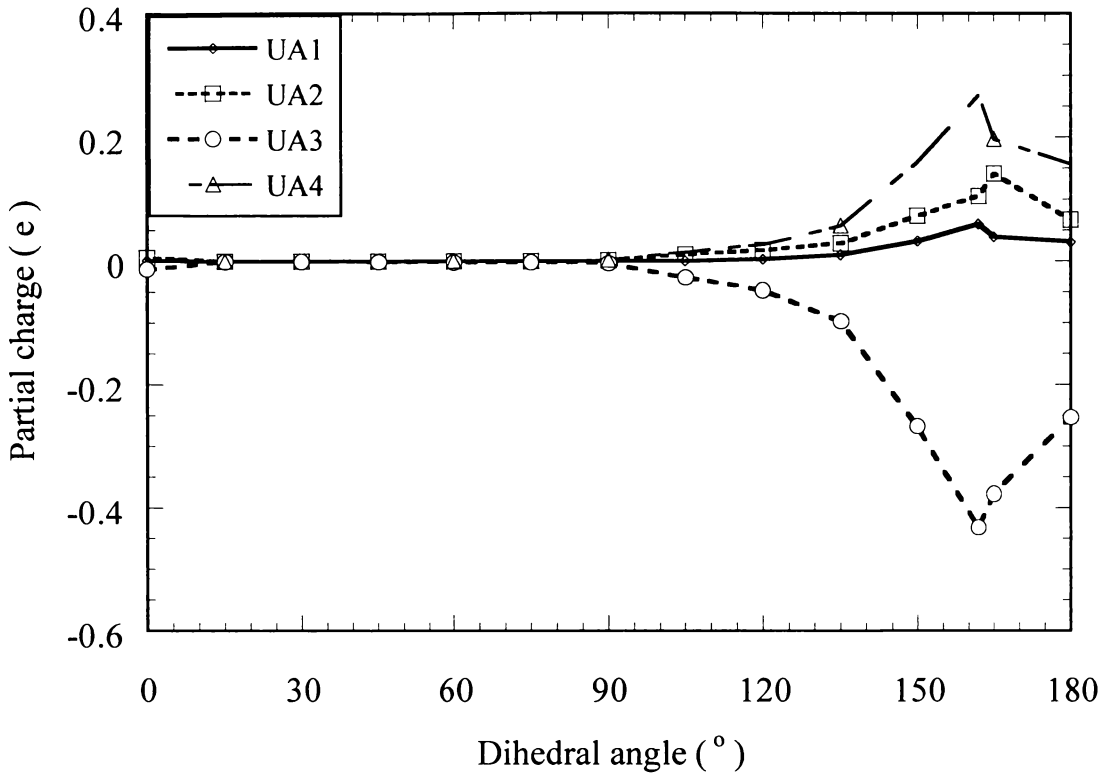


Figure 17. Weighted united atom partial charge profile along dihedral angle C-C-O-C for perfluoroethylmethylether calculated by the RHF method with the cc-pvdz basis set.

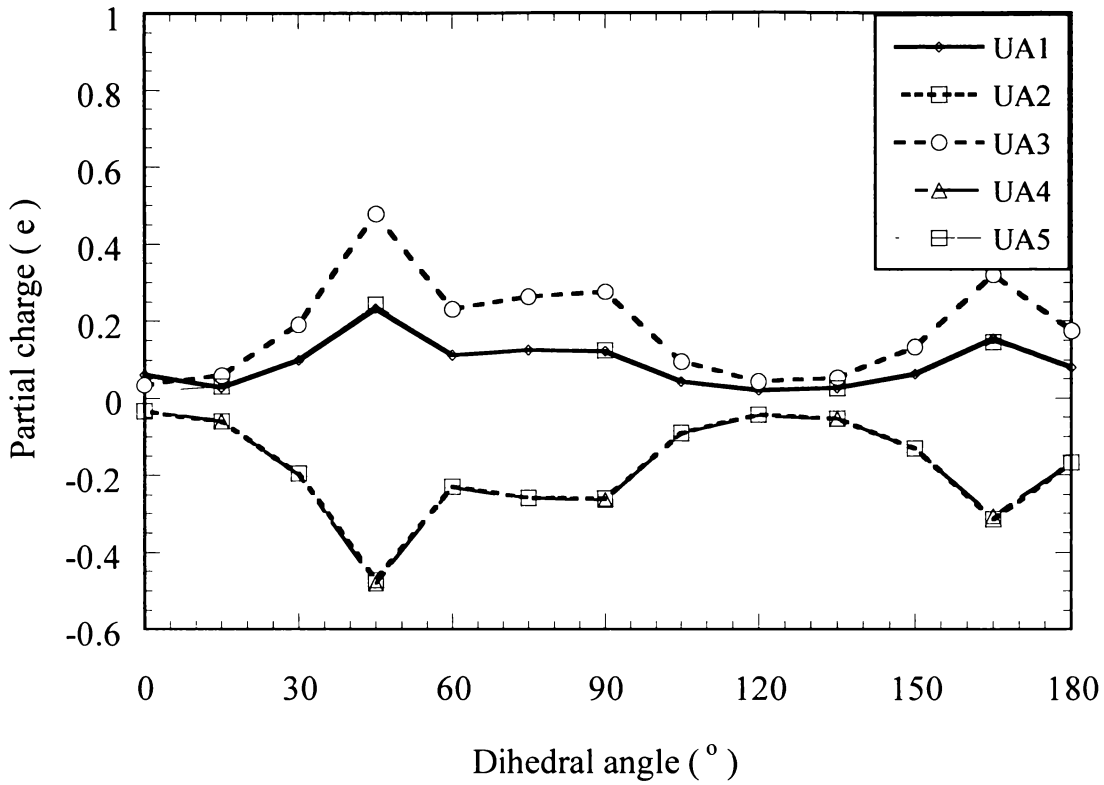


Figure 18. Weighted united atom partial charge profile along dihedral angle C-O-C-O for perfluorodimethoxymethane calculated by the RHF method with the cc-pvdz basis set.

electrostatic interaction and hence jeopardize the validity of the later obtained Lennard-Jones parameters. Therefore, the partial charges fitted specifically to each molecule have been adopted here and are also suggested for other short perfluoroethers. Later in this section, a set of partial charges generalized for long-chain molecules will be suggested. However, it needs to be tested once experimental data are available.

3.2 Fitting Lennard-Jones parameters to phase diagrams

The search for the Lennard-Jones parameters for united atoms in perfluoroethers started with the molecule perfluoromethylpropylether because it should share all the Lennard-Jones parameters needed for the shorter perfluoroethylmethylether. To maintain the transferability of Lennard-Jones parameters from perfluoroalkanes to perfluoroethers, initially all the CF_x parameters have been kept the same as their original values [82]. The optimization from this basis led to a set of parameters for oxygen with σ_O = 3.0698 Å and ε_O/k = 125 K, where k is the Boltzmann constant. This Lennard-Jones parameter set will subsequently be referred as the 'first' parameter set.

Figure 19 shows the comparison of the phase envelope from the simulation with the first parameter set and that from experiment for perfluoromethylpropylether. In the figure, the simulation results agree well with the experimental data, which is not surprising since the first parameter set was obtained by fitting the simulated phase envelope to the experimental one. Figure 20 shows the comparison of the phase envelope from the simulation with the first parameter set and that from experiment for

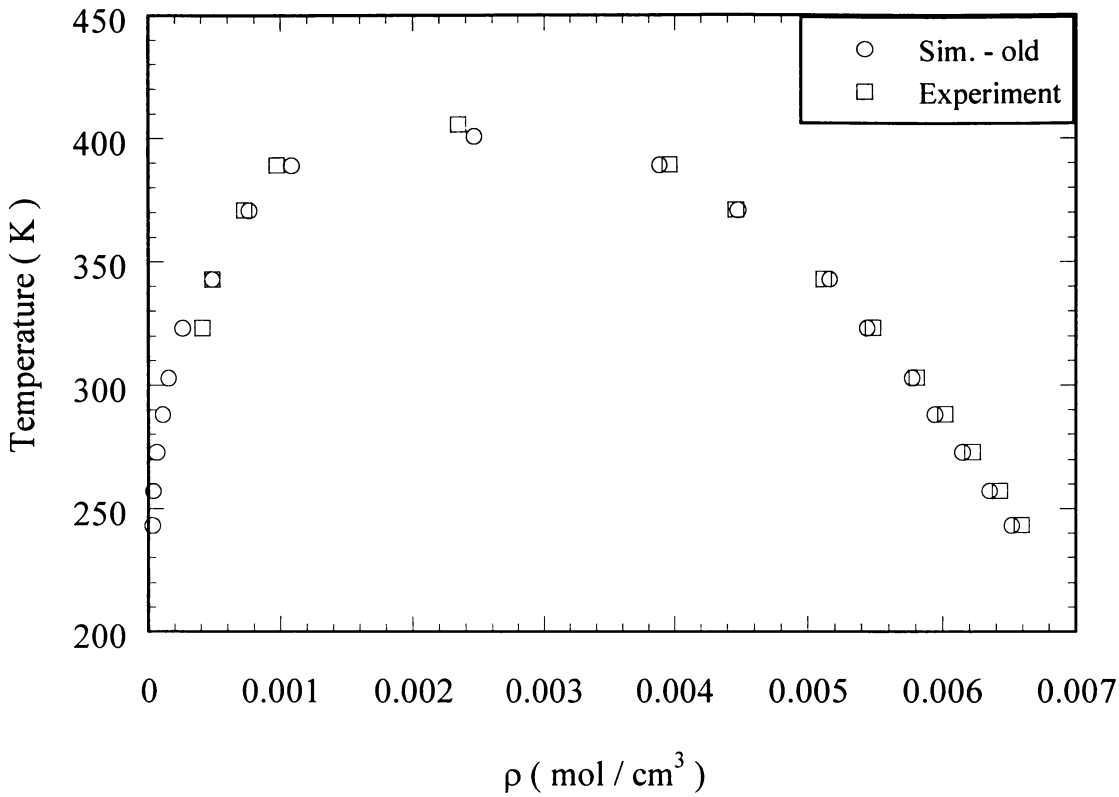


Figure 19. Phase diagram of perfluoromethylpropylether from simulation with first parameter set and experiment [21].

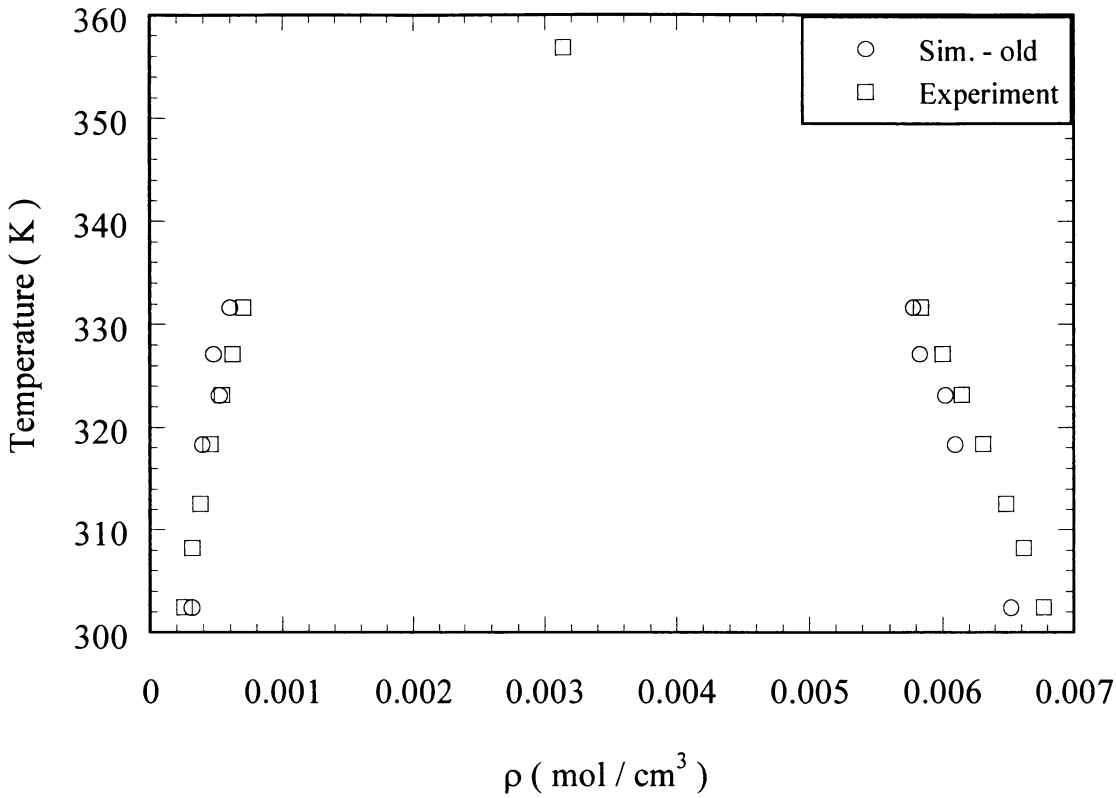


Figure 20. Phase diagram of perfluoroethylmethylether from simulation with first parameter set and experiment [100].

perfluoroethylmethylether. The phase envelope from the simulation is again close to the one from experiment, which suggests that the Lennard-Jones parameters for oxygen obtained by fitting to the experimental data of perfluoromethylpropylether are adequate. However, the effort to apply the same parameter set to perfluorodimethoxymethane failed, as might be expected since the introduction of two oxygen atoms should be expected to affect the Lennard-Jones parameters of the central CF_2 in CF_3-O-CF_2-O-CF_3. To fix this problem, the Lennard-Jones parameters for the CF_x site next to oxygen were allowed change to provide the extra degrees of freedom needed.

The re-parameterization started with fitting the parameters for perfluoromethylpropylether and perfluoroethylmethylether at the same time. The Gibbs-Duhem integration technique was applied during this process. There are two major simplifications in the Gibbs-Duhem integration. One of them is that the calculation of the dependence of the phase envelope on the Lennard-Jones parameters is only performed at one temperature. The effect of this simplification is discussed in appendix B. The other is that the new parameters generated from the technique are obtained by shifting the liquid branch of the simulated phase envelope to the experimental one. Because of these two simplifications, the technique could not generate a more precise set of new parameters, and hence could not perform well on fine-tuning the parameters. For fine-tuning parameters, the technique can be improved by carrying out the calculation of the phase envelope dependence at more state points as explained in appendix B. However, during the fine-tuning of the parameters, this approach may not improve the efficiency at all. As can be seen in figures 19 and 20, the

first parameter set already closely reproduces the experimental phase envelope; therefore, the Gibbs-Duhem integration technique does not work very well here.

Without the Gibbs-Duhem integration technique, the new set of the Lennard-Jones parameters was obtained by trial and error. Since the first parameter set performs well, it was not necessary to change many parameters. At the end of the optimization process, only the σ of CF_2 was changed by reducing it to 4.45 Å. This is not unreasonable because the introduction of the oxygen atom reduces the steric hindrance and allows the CF_2 group to adjust to the approaching interaction site and, hence, the CF_2 group shows a smaller apparent size parameter. It is also reasonable that the σ of CF_3 was not changed because CF_3 is the end group, and, without the hindrance from one side, it should be flexible enough whether the oxygen is introduced or not. Figures 21 and 22 show the comparison of the simulated and experimental phase envelopes for perfluoromethylpropylether and perfluoroethylmethylether, respectively, with the final parameter set. Although the final parameter set does not improve the performance of simulation for perfluoroethylmethylether, it does show improvement for simulating perfluoromethylpropylether especially on the critical properties.

With the parameters of CF_3 fixed and unchanged after the optimization process for perfluoroethylmethylether and perfluoromethylpropylether, the σ and ε/k parameters for the central CF_2 site were the only adjustable parameters during the parameter optimization for perfluorodimethoxymethane. With the original parameters for the CF_2 site, the simulation severely overestimated the saturated liquid densities.

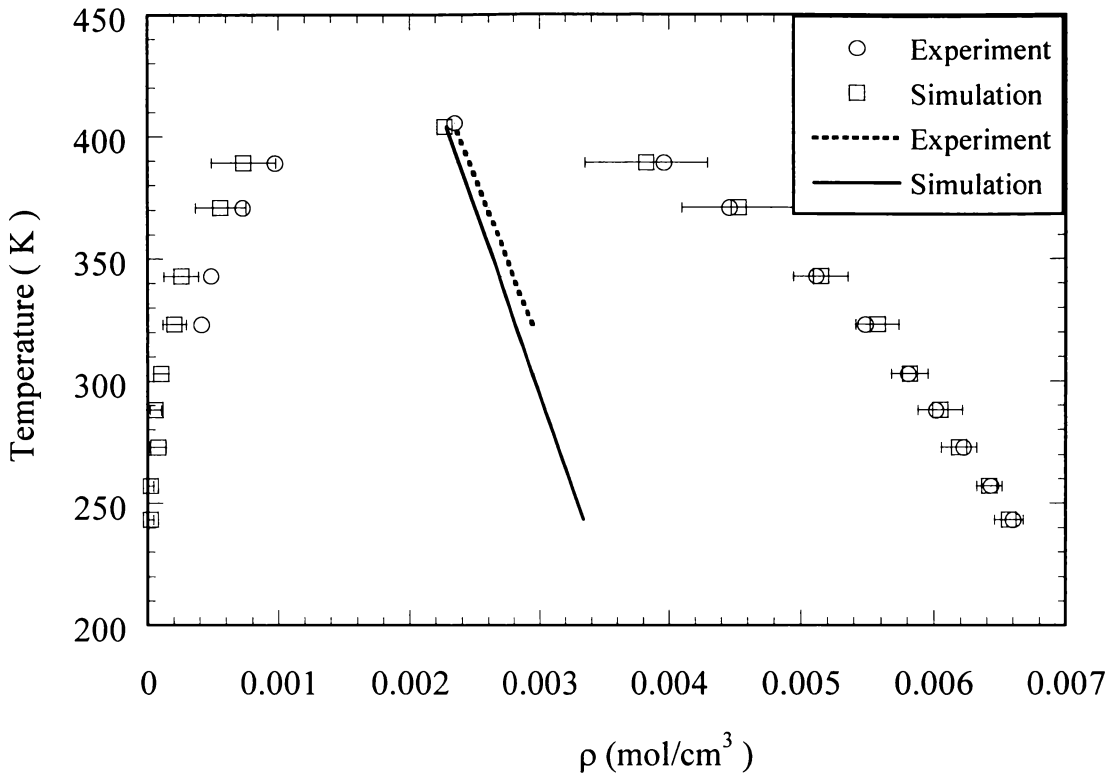


Figure 21. Phase diagram of perfluoromethylpropylether from simulation with the final parameter set and experiment [21]. The solid and dotted lines are the rectilinear lines from simulation and experiment respectively.

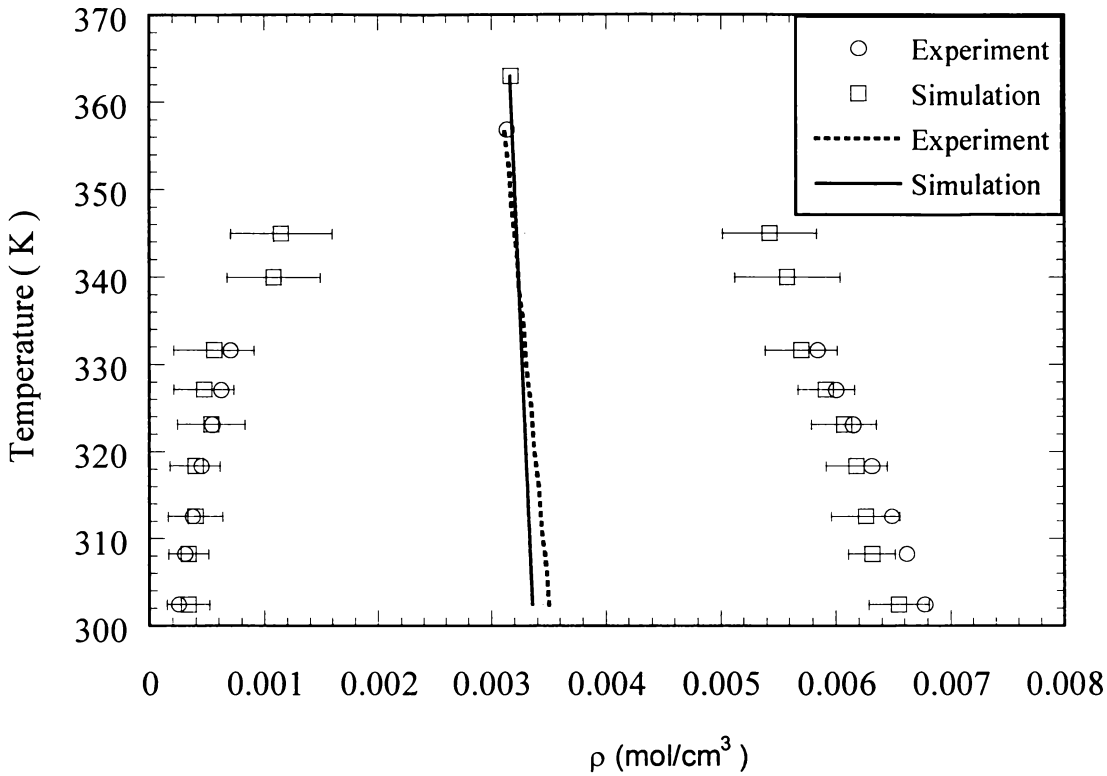


Figure 22. Phase diagram of perfluoroethylmethylether from simulation with the final parameter set and experiment [100]. The solid and dotted lines are the rectilinear lines from simulation and experiment respectively.

The Gibbs-Duhem integration technique was again applied to provide a new set of parameters, and it quickly adjusted the parameters from 4.6 Å and 30 K to 5.36 Å and 24 K for σ and ε/k, respectively, at first trial. This optimization process is particular difficult and a variety of combinations of σ and ε/k have shown similar performance on the phase envelope, indicating strong cross-correlation between them. For example, at a temperature of 302 K, with σ and ε/k equal to 5.6 Å and 18 K, the simulated saturated densities are 0.00620 (mol/cm^3) and 0.00015 (mol/cm^3) for liquid and vapor respectively which are only slightly different from the values from the final optimized set at 0.00640 (mol/cm^3) and 0.00017 (mol/cm^3). This shows that the Gibbs-Duhem integration technique without modification can provide the correct direction and closely approach the region of the optimized parameters.

As previously mentioned, there is a wide range of choice of parameters for the central CF_2 in CF_3-O-CF_2-O-CF_3 ranging from a very large σ and a moderately small ε/k to a relatively large σ and a very small ε/k. One possible explanation for this cross-correlation is that the long-range interaction with this CF_2 site is mostly accounted for by the electrostatic potential (recall that the partial charge on it has a relative high value at -0.48*e* compared to the other CF_x) and the short-range repulsive interaction of this central site is shielded by the O-CF_3 groups on either side. Therefore, a combination of a small ε/k and a comparably smaller σ seems appropriate, and hence the parameters have been chosen to be 5.0 Å and 2.5 K.

Figure 23 shows the comparison of the phase diagram obtained from experiment and from the simulation with the final parameter set. This parameter set does well on the vapor branch of the phase envelope. On the liquid side, it does better at mid-temperature, underestimates the densities at low temperature, and overestimates at high temperature. Hence, the critical temperature is also overestimated and critical density is underestimated. This suggests that a more exact, but not transferable, parameter set for this molecule might have higher ε/k and lower σ parameters.

From the performance of the Gibbs-Duhem integration technique above, it is concluded that the current technique can speed up the parameter search at the initial stage; however, at the later fine-tuning stage, it is not as valuable as expected. The Gibbs-Duhem integration technique is still a useful tool especially with its potential in automating the parameter searching process.

To summarize this section, a united atom potential model has been developed in this work. The model was first developed for a single molecule, perfluoromethylpropylether, (accepted for publication) and then extended to other molecules. The initial model, with only oxygen parameters adjustable, has been shown to be applicable to a similar molecule, perfluoroethylmethylether. This is a verification of the oxygen parameters. The extension of the potential model was carried out with the help of the Gibbs-Duhem integration technique. The Gibbs-Duhem integration technique has been shown to be an efficient tool to quickly bring Lennard Jones parameters their respective optimized regions and could be a tool for automating the

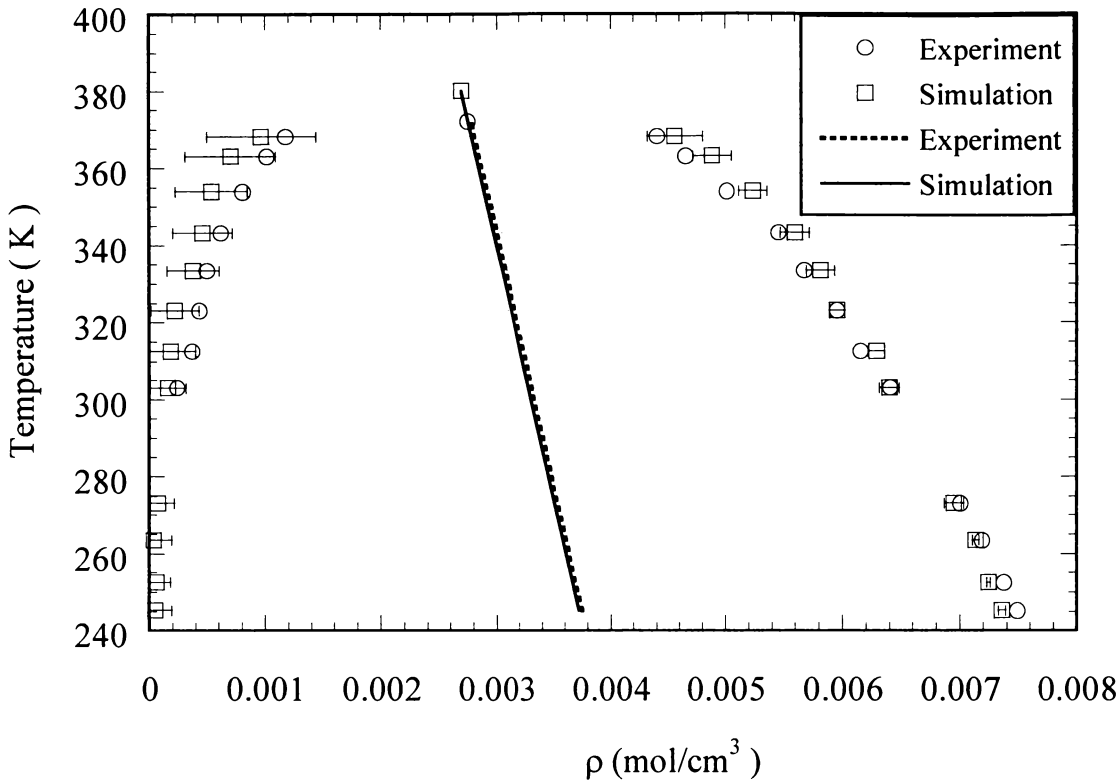


Figure 23. Phase diagram of perfluorodimethoxymethane from simulation with the final parameter set and experiment [20, 21]. The solid and dotted lines are the rectilinear lines from simulation and experiment respectively.

parameterizing process, which is now done by trial and error. Table 2 lists the critical properties for the modeled molecules from the simulation and the experiment. The critical properties from the simulation agree reasonably well with those from the experiment especially for perfluoromethylpropylether.

Table 3 lists the final parameters for all the potentials including the intra- and inter-molecular potentials. Note that the partial charges for these small molecules are not generalized, as previously mentioned. For long chain molecules, the generalized set derive from the partial charges of the modeled molecules might be useful. However, further testing is needed.

Table 2. Critical properties of the modeled molecules.

Molecule*	PFEME	PFMPE	PFDMM
Critical temperature (K)			
Simulation	363.05	404.47	380.14
Experiment	356.85	405.81	372.30
Critical density (mol/cm^3)			
Simulation	0.003168	0.002266	0.002696
Experiment	0.003137	0.002343	0.002750

* Abbreviations:
PFEME: perfluoroethylmethylether
PFMPE: perfluoromethylpropylether
PFDMM: perfluorodimethoxymethane

Table 3. Parameters of the potential model for perfluoroethers.

Potential	Model	Parameters
Stretching	Fixed	C-C 1.536 Å C-O 1.360 Å
Bending	$E_{ba} = \sum_{angles} K_\theta (\theta - \theta_{eq})^2$	θ_{eq} (°): C-C-C 116.71 C-C-O 109.13 C-O-C 121.69 O-C-O 108.61 K_θ (kj mol^{-1} rad^{-2}): C-C-C 428.32 C-C-O 455.89 C-O-C 281.38 O-C-O 806.65
Torsional	$E_{torsion} = \sum_{Di} \sum_{i=0}^{7} a_i \cdot \cos^i(\phi)$	C-C-C-O (kj mol^{-1}): a_0 = 6.5728 a_1 = -22.891 a_2 = 10.802 a_3 = 22.665 a_4 = -26.185 a_5 = 15.312 a_6 = 17.718 a_7 = -7.0944 C-C-O-C (kj mol^{-1}): a_0 = 8.4719 a_1 = 9.9988 a_2 = -12.342 a_3 = -49.346 a_4 = 21.799 a_5 = 111.320 a_6 = -3.3242 a_7 = -59.017 C-O-C-O (kj mol^{-1}): a_0 = 2.0217 a_1 = -4.5680 a_2 = 23.512 a_3 = -24.087 a_4 = -62.659 a_5 = 66.910 a_6 = 42.541 a_7 = -35.266

Table 3. continued

Potential	Model	Parameters
Partial Charge*	$E_{es} = \frac{1}{4\pi\varepsilon_0}\frac{\overline{q_i q_j}}{r}$	C – C – C – O - C 0.08 -0.11 0.20 -0.42 0.25 C – C – O - C 0.05 -0.13 -0.42 0.24 C – O – C – O - C 0.24 -0.48 0.48 -0.48 0.24
L-J	$E_{vdw} = 4\varepsilon\left[\left(\frac{\sigma}{r}\right)^{12} - \left(\frac{\sigma}{r}\right)^{6}\right]$	σ (Å): CF_2 4.6 CF_3 4.6 O 3.0698 CF_2** 4.45 CF_2*** 5.0 ε/k (K): CF_2 30 CF_3 79 O 125 CF_2** 30 CF_2*** 2.5

* Generalized partial charge set suggested for long-chain perfluoroethers (not tested):

CF_3 - CF_2 - CF_x – O - CF_x

0.08 -0.08 0.24 -0.48 0.24

For long-chain perfluoroethers, only the CF_x sites next to the end or at the end and those next to oxygen are assigned partial charges. The rest are zero charged as in perfluoroalkanes. And the net partial charge on a particular site is the sum of all the contributions.

** CF_2 site next to one oxygen atom

*** CF_2 site surrounded by two oxygen atoms

CHAPTER 4

CONCLUSIONS AND RECOMMENDATIONS

A potential model for perfluoroethers based on available phase equilibrium data has been developed and shown to reproduce the experimental phase envelopes and the critical properties reasonably well. Gibbs ensemble simulation with this potential model was the first phase equilibrium simulation for perfluoroethers. Parameters for CF3 and CF4 groups not adjacent to oxygen which were previously developed for perfluoroalkanes have been retained so that the potential model may have the greatest transferability. In addition, a set of generalized partial charges for sites in larger perfluoroethers has been proposed but not tested.

During the process, the Gibbs-Duhem integration technique has been extended for simultaneous parameter optimization on several molecules; this technique has been used to help the efficiency of parameter optimization. However, because of the assumptions and simplifications in the current technique, it is not a precise tool yet, but it may be of considerable use in locating the region of the optimal parameter set. It may not be efficient or economic to further refine the technique; however, it does provide an

approach to automate the parameter optimization process. It will be interesting to use this technique for developing other potential models and to automate the process.

The number of perfluoroether compounds used in the process is limited by the limited experimental data. If more experimental data are available, it will also be interesting to test the potential model on other compounds especially long-chain molecules. It may also be of interest to use this model to predict thermodynamic properties and compare them with the existing data to further verify the model. Furthermore, the model can be used in realistic simulations of several applications of perfluoroethers such as the lubrication and micelle formation with water in supercritical carbon dioxide.

Specific recommendations for further work include the following:

1. Further verify the potential model by calculating other thermodynamic properties such as vapor pressure. Although such calculations are not necessarily the measuring stick of a potential model, they would indicate the applicability of this potential model to a broader field.
2. Test the potential model on long-chain molecules when experimental data are available. This extension would assure the applicability of this potential model to polymers of perfluoroethers which are among several entries of the application list.
3. Apply the potential model for perfluoroethers to realistic simulations such as lubrication. As a matter of fact, this part of work is already underway. This potential model is now applied to the calculations of viscous properties of

perfluoroethers under shear to study the modeled molecules as lubricants. Also, this potential model allows the simulation of the reverse micelle system to be carried out with more interesting surfactants, perfluoroethers.

4. Develop an explicit atom potential model for perfluoroethers. For dynamic properties, such a model is usually necessary for accuracy beyond the qualitative level, and spectroscopic data if available would be a valuable tool to refine it.
5. Further refine the Gibbs-Duhem integration technique and use it to automate the parameterization process. With further refinement, such a tool could change the way parameterization of potential models is normally done.

BIBLIOGRAPHY

Bibliography

[1] Kroschwitz, J.I. and Howe-Grant, M.,1991, *Encyclopedia of Chemical Technology.* 4th ed. Vol. **11**. (New York: Wiley), pp. 499-504.

[2] May, G., 1997, *Chemistry in Britain*, **August** 34-36.

[3] Rudnick, L.R. and Shubkin, R.L.,1999, *Synthetic Lubricants and High Performance Functional Fluids*. Chemical Industry Series. Vol. **77**. (Marcel Dekker).

[4] Schwartz, M., 1997, *Journal of Fluorine Chemistry*, **83**, 9-13.

[5] Bartz, W.J., 1992, *Lubrication Engineering*, **48**(1), 765-774.

[6] Sadeghi, F., Trope, E.J., and Schnell, T.J., 1996, *Tribolology Transactions*, **39**(4), 849-854.

[7] Hamada, T., 2000, *Physical Chemistry Chemical Physics*, **2**, 115-122.

[8] Ma, X., Gui, J., Smoliar, L., Grannen, K., Marchon, B., Bauer, C.L., and Jhon, M., S,, 1999, *Physical Review E.*, **59**(1), 722-727.

[9] Nakakawaji, T., Ishida, M., Ito, Y., Matsumoto, H., Tani, H., and Ishihara, H., 2000, *Tribology Transactions*, **43**(4), 671-676.

[10] Waltman, R.J., 2000, *Chem. Mater.*, **12**, 2039-2049.

[11] Toselli, M., Messori, M., Bongiovanni, R., Malucelli, G., Priola, A., Pilati, F., and Tonelli, C., 2001, *Polymer*, **42**(5), 1771-1779.

[12] Thanawala, S.K. and Chaudhury, M.K., 2000, *Langmuir*, **16**(3), 1256-1260.

[13] Bongiovanni, R., Malucelli, G., Pollicino, A., Tonelli, C., Simeone, G., and Priola, A., 1998, *Macromolecular Chemistry and Physics*, **199**(6), 1099-1105.

[14] Priola, A., Bongiovanni, R., Malucelli, G., Pollicino, A., Tonelli, C., and Simeone, G., 1997, *Macromolecular Chemistry and Physics*, **198**(6), 1893-1907.

[15] Tonelli, C., Trombetta, T., Scicchitano, M., Simeone, G., and Ajroldi, G., 1996, *Journal of Applied Polymer Science*, **59**(2), 311-327.

[16] Pantini, G., Forestieri, R., Brunetta, F., and Bencini, P.L., 1990, *International Journal of Cosmetic Science*, **12**(6), 273-279.

[17] Johnson, G., Meijs, G.F., Laycock, B.G., Griffith, M.G., Chaouk, H., and Steele, J.G., 1999, *Journal of Biomaterials Science-Polymer Edition*, **10**(2), 217-233.

[18] Moreira, H., Dequeiroz, J.M., Liggett, P.E., and McDonnell, P.J., 1992, *Cornea*, **11**(5), 376-379.

[19] Johnston, K.P., Randolph, T., Bright, F., and Howdle, S., 1996, *Science*, **272**, 1726-1726.

[20] Wang, B.-H., Adcock, J.L., Mathur, S.B., and Van Hook, W.A., 1991, *J. Chem. Therm.*, **23**(7), 699-710.

[21] Salvi-Narkhede, M., Adcock, J.L., Gakh, A., and Van Hook, W.A., 1993, *J. Chem. Therm.*, **25**(5), 643-647.

[22] Cece, A., Jureller, S.H., Kerschner, J.L., and Moschner, K.F., 1996, *Journal of Physical Chemistry*, **100**(18), 7435-7439.

[23] Johnston, K.P., Harrison, K.L., Clarke, M.J., Howdle, S.M., Heiltz, M.P., Bright, F.V., Carlier, C., and Randolph, T.W., 1996, *Science*, **271**, 624-626.

[24] Beckman, E.J., 1996, *Science*, **272**, 613-614.

[25] Eastoe, J., Bayazit, Z., Martel, S., Steytler, D.C., and Heenan, R.K., 1996, *Langmuir*, **12**(6), 1423-1424.

[26] Salaniwal, S., Cui, S.T., Cummings, P.T., and Cochran, H.D., 1999, *Langmuir*, **15**(16), 5188-5192.

[27] Berendsen, H.J.C., Grigera, J.R., and Straatsma, T.P., 1987, *Journal of Physical Chemistry*, **91**(24), 6269-6271.

[28] Jorgensen, W.L., 1982, *Journal of Chemical Physics*, **77**(8), 4156-4163.

[29] Jorgensen, W.L., 1981, *Journal of the American Chemical Society*, **103**(2), 335-340.

[30] Harris, J.G. and Yung, K.H., 1995, *Journal of Physical Chemistry*, **99**(31), 12021-12024.

[31] Weiner, P.K. and Kollman, P.A., 1981, *Journal of Computational Chemistry*, **2**(3), 287-303.

[32] Pearlman, D.A., Case, D.A., Caldwell, J.W., Ross, W.S., Cheatham, T.E., Debolt, S., Ferguson, D., Seibel, G., and Kollman, P., 1995, *Computer Physics Communications*, **91**(1-3), 1-41.

[33] Weiner, S.J., Kollman, P.A., Case, D.A., Singh, U.C., Ghio, C., Alagona, G., Profeta, S., and Weiner, P., 1984, *Journal of the American Chemical Society*, **106**(3), 765-784.

[34] Weiner, S.J., Kollman, P.A., Nguyen, D.T., and Case, D.A., 1986, *Journal of Computational Chemistry*, **7**(2), 230-252.

[35] Cornell, W.D., Cieplak, P., Bayly, C.I., Gould, I.R., Merz, K.M., Ferguson, D.M., Spellmeyer, D.C., Fox, T., Caldwell, J.W., and Kollman, P.A., 1995, *Journal of the American Chemical Society*, **117**(19), 5179-5197.

[36] Jorgensen, W.L. and Swenson, C.J., 1985, *Journal of the American Chemical Society*, **107**(6), 1489-1496.

[37] Jorgensen, W.L., Madura, J.D., and Swenson, C.J., 1984, *Journal of the American Chemical Society*, **106**(22), 6638-6646.

[38] Jorgensen, W.L. and Nguyen, T.B., 1993, *Journal of Computational Chemistry*, **14**(2), 195-205.

[39] Jorgensen, W.L. and Tiradorives, J., 1988, *Journal of the American Chemical Society*, **110**(6), 1666-1671.

[40] Jorgensen, W.L., Maxwell, D.S., and TiradoRives, J., 1996, *Journal of the American Chemical Society*, **118**(45), 11225-11236.

[41] Brooks, B.R., Bruccoleri, R.E., Olafson, B.D., States, D.J., Swaminathan, S., and Karplus, M., 1983, *Journal of Computational Chemistry*, **4**(2), 187-217.

[42] MacKerell, A.D., Bashford, D., Bellott, M., Dunbrack, R.L., Evanseck, J.D., Field, M.J., Fischer, S., Gao, J., Guo, H., Ha, S., Joseph-McCarthy, D., Kuchnir, L., Kuczera, K., Lau, F.T.K., Mattos, C., Michnick, S., Ngo, T., Nguyen, D.T., Prodhom, B., Reiher, W.E., Roux, B., Schlenkrich, M., Smith, J.C., Stote, R., Straub, J., Watanabe, M., Wiorkiewicz-Kuczera, J., Yin, D., and Karplus, M., 1998, *Journal of Physical Chemistry B*, **102**(18), 3586-3616.

[43] Smith, J.C. and Karplus, M., 1992, *Journal of the American Chemical Society*, **114**(3), 801-812.

[44] Mulliken, R.S., 1955, *Journal of Chemical Physics*, **23**, 1833-1840.

[45] Dauber-Osguthorpe, P., Roberts, V.A., Osguthorpe, D.J., Genest, M., and Hagler, A.T., 1988, *Proteins: Struct., Funct., Genet.*, **4**(1), 31-47.

[46] Halgren, T.A., 1992, *Journal of the American Chemical Society*, **114**(20), 7827-7843.

[47] Panagiotopoulos, A.Z., 1987, *Molecular Physics*, **61**(4), 813-826.

[48] Kofke, D.A., 1993, *Molecular Physics*, **78**(6), 1331-1336.

[49] Frisch, M.J., Trucks, G.W., Schlegel, H.B., Scuseria, G.E., Robb, M.A., Cheeseman, J.R., Zakrzewski, V.G., Montgomery, J.A.J., Stratmann, R.E., Burant, J.C., Dapprich, S., Millam, J.M., Daniels, A.D., Kudin, K.N., Strain, M.C., Farkas, O., Tomasi, J., Barone, V., Cossi, M., Cammi, R., Mennucci, B., Pomelli, C., Adamo, C., Clifford, S., Ochterski, J., Petersson, G.A., Ayala, P.Y., Cui, Q., Morokuma, K., Malick, D.K., Rabuck, A.D., Ragha-vachari, K., Foresman, J.B., Cioslowski, J., Ortiz, J.V., Baboul, A.G., Stefanov, B.B., Liu, G., Liashenko, A., Piskorz, P., Komaromi, I., Gomperts, R., Martin, R.L., Fox, D.J., Keith, T., Al-Laham, M.A., C. Peng, Y., Nanayakkara, A., Gonzalez, C., Challacombe, M., Gill, P.M.W., Johnson, B., Chen, W., Wong, M.W., Andres, J.L., Gonzalez, C., Head-Gordon, M., Replogle, E.S., and Pople, J.A., *Gaussian 98*. 1998, Gaussian, Inc., Pittsburgh PA,.

[50] de Pablo, J.J., 1995, *Fluid Phase Equilibria*, **104**, 195-206.

[51] Collazo, N., Shin, S., and Rice, S.A., 1992, *J. Chem. Phys.*, **96**, 4735-4742.

[52] Shin, S., Collazo, N., and Rice, S.A., 1992, *J. Chem. Phys.*, **96**(2), 1352-1366.

[53] Singh, U.C. and Kollman, P.A., 1984, *J. Comp. Chem.*, **5**(2), 129-145.

[54] Cox, S.R. and Williams, D.E., 1981, *J. Comp. Chem.*, **2**(3), 304-323.

[55] Momany, F.A., 1978, *J. Phys. Chem.*, **82**(5), 592-601.

[56] Bayly, C.I., Ciepak, P., Cornell, W.D., and Kollman, P.A., 1993, *J. Phys. Chem.*, **97**, 10269-10280.

[57] Reynolds, C.A., Essex, J.W., and Richards, W.G., 1992, *Chem. Phys. Lett.*, **199**(3-4), 257-260.

[58] Reynolds, C.A. and Essex, J.W., 1992, *J. Am. Chem. Soc.*, **114**, 9075-9079.

[59] Stone, A.J., 1981, *Chem. Phys. Lett.*, **83**(2), 233-239.

[60] Chipot, C., Angyan, J.G., Ferenczy, G.G., and Scheraga, H.A., 1993, *J. Phys. Chem.*, **97**, 6628-6636.

[61] Ferenczy, G.G., 1991, *J. Comp. Chem.*, **12**(8), 913-917.

[62] Besler, B.H., Merz, K.M., Jr., and Kollman, P.A., 1990, *J. Comp. Chem.*, **11**(4), 431-439.

[63] Panagiotopoulos, A.Z., 1989, *Acs Symposium Series*, **406**, 39-51.

[64] Panagiotopoulos, A.Z., 1992, *Fluid Phase Equilibria*, **76**, 97-112.

[65] Depablo, J.J., Bonnin, M., and Prausnitz, J.M., 1992, *Fluid Phase Equilibria*, **73**(3), 187-210.

[66] Siepmann, J.I. and Frenkel, D., 1992, *Molecular Physics*, **75**(1), 59-70.

[67] Frenkel, D., Mooij, G., and Smit, B., 1992, *Journal of Physics-Condensed Matter*, **4**(12), 3053-3076.

[68] Depablo, J.J., Laso, M., and Suter, U.W., 1992, *Journal of Chemical Physics*, **96**(3), 2395-2403.

[69] Depablo, J.J., Laso, M., and Suter, U.W., 1992, *Journal of Chemical Physics*, **96**(8), 6157-6162.

[70] Wick, C.D. and Siepmann, J.I., 2000, *Macromolecules*, **33**(19), 7207-7218.

[71] Mon, K.K. and Binder, K., 1992, *Journal of Chemical Physics*, **96**(9), 6989-6995.

[72] Recht, J.R. and Panagiotopoulos, A.Z., 1993, *Molecular Physics*, **80**(4), 843-852.

[73] Wilding, N.B., 1995, *Physical Review E*, **52**(1), 602-611.

[74] Bruce, A.D., 1997, *Physical Review E*, **55**(3), 2315-2320.

[75] Valleau, J.P., 1998, *Journal of Chemical Physics*, **108**(7), 2962-2966.

[76] Siepmann, J.I., Karaborni, S., and Smit, B., 1993, *Nature*, **365**(6444), 330-332.

[77] Smit, B., Karaborni, S., and Siepmann, J.I., 1995, *Journal of Chemical Physics*, **102**(5), 2126-2140.

[78] Siepmann, J.I., Martin, M.G., Mundy, C.J., and Klein, M.L., 1997, *Molecular Physics*, **90**(5), 687-693.

[79] VanLeeuwen, M.E., 1996, *Molecular Physics*, **87**(1), 87-101.

[80] Cui, S.T., Cummings, P.T., and Cochran, H.D., 1997, *Fluid Phase Equilibria*, **141**(1-2), 45-61.

[81] Mackie, A.D., Tavitian, B., Boutin, A., and Fuchs, A.H., 1997, *Molecular Simulation*, **19**(1), 1-15.

[82] Cui, S.T., Siepmann, J.I., Cochran, H.D., and Cummings, P.T., 1998, *Fluid Phase Equilibria*, **146**(1-2), 51-61.

[83] Cui, S.T., Cochran, H.D., and Cummings, P.T., 1999, *Journal of Physical Chemistry B*, **103**(21), 4485-4491.

[84] Martin, M.G. and Siepmann, J.I., 1998, *Journal of Physical Chemistry B*, **102**(14), 2569-2577.

[85] Martin, M.G. and Siepmann, J.I., 1999, *Journal of Physical Chemistry B*, **103**(21), 4508-4517.

[86] Wick, C.D., Martin, M.G., and Siepmann, J.I., 2000, *Journal of Physical Chemistry B*, **104**(33), 8008-8016.

[87] Chen, B. and Siepmann, J.I., 1999, *Journal of Physical Chemistry B*, **103**(25), 5370-5379.

[88] Errington, J.R. and Panagiotopoulos, A.Z., 1999, *Journal of Physical Chemistry B*, **103**(30), 6314-6322.

[89] Kofke, D.A., 1993, *Journal of Chemical Physics*, **98**(5), 4149-4162.

[90] Mehta, M. and Kofke, D.A., 1994, *Chemical Engineering Science*, **49**(16), 2633-2645.

[91] Agrawal, R., Mehta, M., and Kofke, D.A., 1994, *International Journal of Thermophysics*, **15**(6), 1073-1083.

[92] Bolhuis, P.G. and Kofke, D.A., 1996, *Physical Review E*, **54**(1), 634-643.

[93] Agrawal, R. and Kofke, D.A., 1995, *Molecular Physics*, **85**(1), 43-59.

[94] Tavares, F.W. and Sandler, S.I., 1997, *AIChE Journal*, **43**(1), 218-231.

[95] Polson, J.M. and Frenkel, D., 1998, *Journal of Chemical Physics*, **109**(1), 318-328.

[96] Agrawal, R. and Kofke, D.A., 1995, *Molecular Physics*, **85**(1), 23-42.

[97] Kofke, D.A.,1999, *Semigrand canonical Monte Carlo simulation; Integration along coexistence lines*. in *Monte Carlo Methods in Chemical Physics*, edited by, Editor^Editors., John Wiley & Sons Inc: New York. p. 405-441.

[98] Sturgeon, J.B. and Laird, B.B., 2000, *Physical Review B*, **62**(22), 14720-14727.

[99] Levine, I.N.,1991, *Quantum Chemistry*. 4 ed., Englewood, New Jersey: Prentice Hall.

[100] Beyerlein, A.L., DesMarteau, D.D., Kul, I., and Zhao, G., 1998, *Fluid Phase Equilibria*, **150-151**, 287-296.

[101] Cochran, H.D., Salaniwal, S., Cui, S.T., and Cummings, P.T., 2000, *Abstracts of Papers of the American Chemical Society*, **220**, 145-COMP.

[102] Salaniwal, S., Cui, S.T., Cochran, H.D., and Cummings, P.T., 2000, *Industrial & Engineering Chemistry Research*, **39**(12), 4543-4554.

[103] Salaniwal, S., Cui, S.T., Cochran, H.D., and Cummings, P.T., 2001, *Langmuir*, **17**(5), 1773-1783.

[104] Salaniwal, S., Cui, S.T., Cochran, H.D., and Cummings, P.T., 2001, *Langmuir*, **17**(5), 1784-1792.

[105] Walton, J.P.R.B. and Gubbins, K.E., 1985, *Molecular Physics*, **55**(3), 679-688.

[106] Thompson, S.M. and Gubbins, K.E., 1984, *Journal of Chemical Physics*, **81**(1), 530-542.

[107] Walton, J.P.R.B. and Gubbins, K.E., 1986, *Molecular Physics*, **58**(5), 1013.

[108] Shreve, A.P., Walton, J.P.R.B., and Gubbins, K.E., 1986, *Journal of Chemical Physics*, **85**(4), 2178-2186.

[109] Fenn, R.,2001, *Geometry*., London: Springer.

APPENDICES

APPENDIX A

MOLECULAR DYNAMICS SIMULATIONS OF REVERSE MICELLES

A.1 Method

As previously mentioned, much attention has been given to the formation and application of the reverse micelles with a water core and with perfluoro compounds as the surfactant in supercritical carbon dioxide. It is important to examine the state of the water core inside the reverse micelles as it may be quite different from that of the bulk system and the conditions of aqueous environment are crucial to applications such as the reacting medium of enzymatic reactions. A previously successful molecular dynamics simulation [26] of Eastoe's system [25] was followed to study the aqueous environment in the water core in terms of the density and pressure tensor profiles and the interfacial tension between the water core and the carbon dioxide solvent.

In the simulations by Salaniwal et al. [26, 101-104], the SPC-E model for water [27], the Harris and Yung model for carbon dioxide [30], the Siepmann et al. model for the alkane tail [76], and the Cui and Siepmann et al. model for the perfluoroalkane tail [82] were adopted. To simulate the experimental system studied by Eastoe, the calculations were done with 33 di-chain surfactant molecules, 1175 water molecules, and 12800 carbon dioxide molecules, a total of 42618 interaction sites. In terms of the

size of the system, such a simulation is difficult even with today's computer power. Therefore, the simulation was parallelized.

One interesting question raised by the simulation results is how different is the aqueous core inside the reverse micelle compared with the bulk system. For applications such as enzymatic reactions, the pH, pressure, ionic strength, etc. of the medium can greatly affect the result, and hence it will be valuable to study in more detail the properties of the water core. Pressure is one of the thermodynamic properties that are expected to be quite different inside and outside the core. The surface tension is one of the defining properties for micellar systems.

In the mid-1980s, Gubbins' group studied the pressure tensor in an inhomogeneous pure fluid and implemented the study with molecular dynamics simulations of liquid drops [105-108]. They first studied the pressure tensor and surface tension in a system with pure spherical molecules [106], and then extended it to pure non-spherical molecules [105, 107, 108]. In their 1985 paper [105], they provided a derivation, which can be summarized as follow:

The pressure of the system, $\mathbf{P}(\mathbf{r})$, comes from both the kinetic and configurational contributions.

$$\mathbf{P}(\mathbf{r}) = \mathbf{P}_K(\mathbf{r}) + \mathbf{P}_C(\mathbf{r}) \tag{A-1}$$

The configurational contribution for a pairwise additive potential can then be written as:

$$\mathbf{P}_C(\mathbf{r}) = -\frac{1}{2}\left\langle \sum_{i \neq j} \sum \frac{\partial u(ij)}{\partial \mathbf{r}_{ij}} \int_{C_{ij}} d\tilde{\mathbf{l}}\, \delta\left(\mathbf{r} - \tilde{\mathbf{l}}\right) \right\rangle \tag{A-2}$$

where the brackets stand for the ensemble average and C_{ij} is an arbitrary contour from i to j across which the forces act. Essentially, what equation A-2 says is that the configurational contribution of the pressure is the ensemble average of the integral of the forces across a contour through which they act.

One of the difficulties in determining the pressure is the selection of the contour, C_{ij}, since it is arbitrary. One straightforward selection is to define the contour as the straight line between i and j, which gives the Irving-Kirkwood expression of the pressure tensor. This definition is shown in the upper part of figure A-1 with black lines. However, the Irving-Kirkwood definition encounters some difficulty in the case demonstrated by the red lines, where it cuts through surface of **r** twice in a spherical system. Therefore, the implementation of the Irving-Kirkwood pressure tensor is not as trivial as one might think. A less obvious choice of the contour, as seen in the lower part of figure A-1, would go from i along the **r** surface to point a (moving in the θ and ϕ directions) and then from a to j, which generates the Harasima expression of the pressure tensor. This choice of contour avoids the double intersection in Irving-Kirkwood contour, and has been adopted in this work.

Following Walton and Gubbins' derivation, the normal and transverse components of the pressure tensor with spherical symmetry for the Harasima contour can be obtained as follows:

$$\mathbf{P}_N(\mathbf{r}) = kT\rho(\mathbf{r}) - \frac{1}{8\pi r^2}\left\langle \sum_{i\neq j}\sum \frac{\tilde{\mathbf{r}}_{ij}}{\left|\tilde{\mathbf{r}}_{ij}\right|}\left(\frac{\partial u(ij)}{\partial \mathbf{r}_{ij}}\cdot \mathbf{e}_r^{(i)}\right)\times \theta\left(\frac{\mathbf{r}-\mathbf{r}_i}{\tilde{\mathbf{r}}_{ij}}\right)\theta\left(\frac{\mathbf{r}_j-\mathbf{r}}{\tilde{\mathbf{r}}_{ij}}\right)\right\rangle \qquad \text{(A-3)}$$

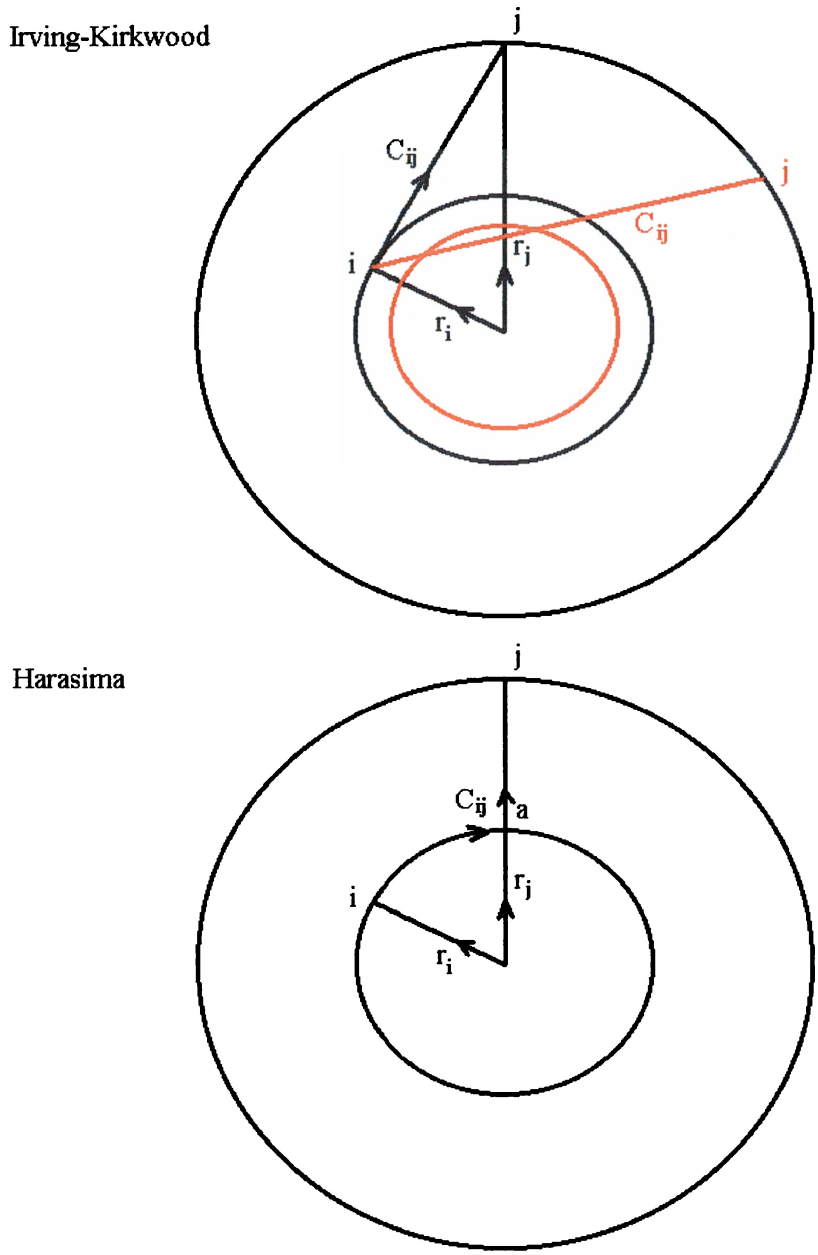


Figure A-1. Definitions of contour, C_{ij}, in the Irving-Kirkwood and Harasima pressure tensor expressions.

$$\mathbf{P}_T(\mathbf{r}) = kT\rho(\mathbf{r}) - \frac{1}{16\pi}\left\langle \sum_{i\neq j}\sum \begin{bmatrix} \left(\mathbf{r}_{ij}\cdot\mathbf{e}_{\theta}^{(i)}\right)\left(\frac{\partial u(ij)}{\partial \mathbf{r}_{ij}}\cdot\mathbf{e}_{\theta}^{(i)}\right) + \\ \left(\mathbf{r}_{ij}\cdot\mathbf{e}_{\phi}^{(i)}\right)\left(\frac{\partial u(ij)}{\partial \mathbf{r}_{ij}}\cdot\mathbf{e}_{\phi}^{(i)}\right) \end{bmatrix} \times \frac{1}{\mathbf{r}_i^2}\delta(\mathbf{r}-\mathbf{r}_i) \right\rangle \qquad \text{(A-4)}$$

where $\tilde{\mathbf{r}}_{ij}$ in equation A-3 is defined as $|\mathbf{r}_j| - |\mathbf{r}_i|$; therefore $\tilde{\mathbf{r}}_{ij} / \left|\tilde{\mathbf{r}}_{ij}\right|$ is positive when j is located outside of i and negative otherwise. Also, the functions θ( ) and δ( ) in equations A-3 and A-4 are the unit step function and Dirac delta function, respectively. Once the normal and transverse components of pressure tensor have been obtained, the following mechanical expression for surface tension, equation A-5, can be used with the Laplace equation, equation A-6, to obtain the surface tension or interfacial tension in the present case.

$$\gamma = \int_0^{\infty}\left(\frac{\mathbf{r}}{\mathbf{r}_s}\right)^2 [\mathbf{P}_N(\mathbf{r}) - \mathbf{P}_T(\mathbf{r})]d\mathbf{r} \qquad \text{(A-5)}$$

$$\Delta\mathbf{P} = \frac{2\gamma}{\mathbf{r}_s} \qquad \text{(A-6)}$$

In previous reverse micelle work, the simulation was carried out in a cubic box in Cartesian coordinates; therefore, to implement equations A-3 and A-4, the expressions for $\left(\mathbf{r}_{ij}\cdot\mathbf{e}_x^{(i)}\right)$, where x stands for r, θ, and ϕ, had to be derived, which is not trivial for the θ and ϕ directions. The derivations for the expressions of $\left(\mathbf{r}_{ij}\cdot\mathbf{e}_x^{(i)}\right)$ in the θ and ϕ directions are shown in next section, and the result for the θ direction obtained is consistent with that provided by Thompson et al. [106].

A.2 IMPLEMENTATION OF PRESSURE PROFILE CALCULATION

To evaluate the pressure tensor without too much extra computation time, it is important to derive the expression of $\left(\mathbf{r}_{ij} \cdot \mathbf{e}_x^{(i)}\right)$ in terms of $\mathbf{r}_{ij}$ and $\mathbf{r}_{Oi}$ in Cartesian coordinates, where O is the origin of the spherical system or, in our case, the center of mass of the aggregate, because this information is already available. In this section, the expression is derived. Before starting the derivation, a mathematical tool [109] must be introduced, as follow:

Let **A** be a unit vector, **A** = (u, v, w), and O be the origin. The matrix **M**,

$$\mathbf{M} = \begin{bmatrix} \cos\theta + u^2(1-\cos\theta) & uv(1-\cos\theta) + w\sin\theta & wu(1-\cos\theta) - v\sin\theta \\ uv(1-\cos\theta) - w\sin\theta & \cos\theta + v^2(1-\cos\theta) & vw(1-\cos\theta) + u\sin\theta \\ wu(1-\cos\theta) + v\sin\theta & vw(1-\cos\theta) - u\sin\theta & \cos\theta + w^2(1-\cos\theta) \end{bmatrix} \quad \text{(A-7)}$$

is orthogonal and represents a rotation about OA through an angle θ.

Let **r** be an arbitrary vector and **r** = (x, y, z). To obtain $\left(\mathbf{r} \cdot \mathbf{e}_\phi^{(i)}\right)$, first shift the origin from O to O' as seen in figure A-2a, and the vector $\mathbf{r}_i$ will become $\mathbf{r}_i$' and $\mathbf{r}_i$' = (x_i, y_i, 0). Then choose **A** = (0, 0, 1) which is along the Z-axis. From figure A-2a, one can see that to obtain $\mathbf{e}_\phi^{(i)}$, one must rotate **r**' along OA for 90 degrees and then normalize the resulting vector. Here, u = 0, v = 0, and w = 1, and θ = 90°. Substituting the values into equation A-7, gives

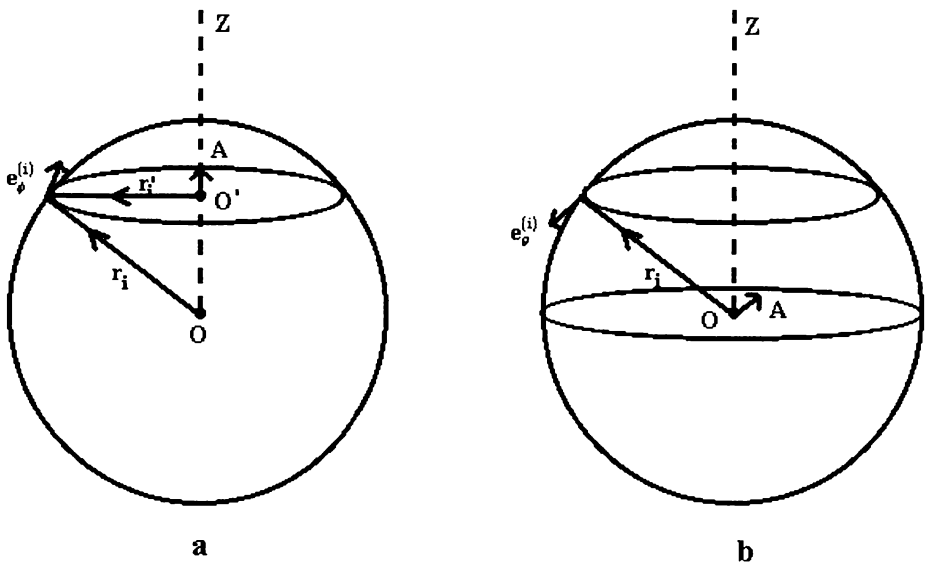


Figure A-2. Schematic representation of $\mathbf{e}_{\phi}^{(i)}$ and $\mathbf{e}_{\theta}^{(i)}$

$$\mathbf{M} = \begin{pmatrix} 0 & 1 & 0 \\ -1 & 0 & 0 \\ 0 & 0 & 1 \end{pmatrix}$$

Then rotating **r'** for 90 degrees by operating with **M** on **r'**, and normalizing the resulting vector gives

$$\mathbf{e}_{\phi}^{(i)} = \frac{1}{\left(x_i^2 + y_i^2\right)^{1/2}} \left(x_i,\ y_i,\ 0 \right) \bullet \begin{pmatrix} 0 & 1 & 0 \\ -1 & 0 & 0 \\ 0 & 0 & 1 \end{pmatrix}$$

$$= \frac{1}{\left(x_i^2 + y_i^2\right)^{1/2}} \left(y_i,\ -x_i,\ 0 \right)$$

Hence $\left(\mathbf{r} \cdot \mathbf{e}_{\phi}^{(i)} \right)$ can be given as follows:

$$\mathbf{r} \cdot \mathbf{e}_{\phi}^{(i)} = \frac{1}{\left(x_i^2 + y_i^2\right)^{1/2}} \left(x y_i - y x_i \right) \tag{A-8}$$

For $\left(\mathbf{r} \cdot \mathbf{e}_{\theta}^{(i)} \right)$, one needs to design an **A**, where **A** should be on the x-y plane and be perpendicular to $\mathbf{r}_i$ as seen in figure A-2b. An obvious choice would be $\mathbf{A} = \frac{1}{\left(x_i^2 + y_i^2\right)^{1/2}} \left(y_i, -x_i, 0 \right)$. Again, one needs to rotate $\mathbf{r}_i$ about OA for 90 degrees and normalize the resulting vector. Substituting the information into the rotation matrix **M** gives

$$\mathbf{M} = \frac{1}{\left(x_i^2 + y_i^2\right)^{1/2}} \begin{pmatrix} y_i^2 & -x_i y_i & x_i \\ -x_i y_i & x_i^2 & y_i \\ -x_i & -y_i & 0 \end{pmatrix}$$

Operating with **M** on $\mathbf{r}_i$ and normalizing the resulting vector gives

$$\mathbf{e}_\theta^{(i)} = \frac{1}{\left(x_i^2 + y_i^2 + z_i^2\right)^{1/2}} \frac{1}{\left(x_i^2 + y_i^2\right)^{1/2}} \left(x_i,\ y_i,\ z_i \right) \bullet \begin{pmatrix} y_i^2 & -x_i y_i & x_i \\ -x_i y_i & x_i^2 & y_i \\ -x_i & -y_i & 0 \end{pmatrix}$$

$$= \frac{1}{\left(x_i^2 + y_i^2 + z_i^2\right)^{1/2}} \frac{1}{\left(x_i^2 + y_i^2\right)^{1/2}} \left(-x_i z_i,\ -y_i z_i,\ x_i^2 + y_i^2 \right)$$

Then,

$$\mathbf{r} \cdot \mathbf{e}_\theta^{(i)} = \frac{1}{\left(x_i^2 + y_i^2 + z_i^2\right)^{1/2}} \frac{1}{\left(x_i^2 + y_i^2\right)^{1/2}} \left[-x_i z_i x - y_i z_i y + \left(x_i^2 + y_i^2\right) z \right] \qquad \text{(A-9)}$$

To implement equation A-4, one simply replaces **r** in equations A-8 and A-9 with $\mathbf{r}_{ij}$ and $\partial u(ij)/\partial \mathbf{r}_{ij}$, and one obtains the transverse component of the pressure profile. The normal component is straightforward; therefore it is not discussed here.

A.3 Pressure profile and interfacial tension

The methods to calculate the pressure tensor and interfacial tension mentioned in section A.1 and A.2 have been implemented in the simulation code by Salaniwal et al. The molecular dynamics simulation has been run for an additional 75 pico-seconds, and the results are shown here. This work is the first calculation of the inhomogeneous pressure tensor in a micellar system, which involves both a mixture of molecules and spherical coordinates, and the first attempt to calculate the transverse component of the inhomogeneous pressure tensor directly in the simulation. It is also the first attempt to calculate the surface tension of a micelle in a molecular simulation.

Figure A-3 shows the number density profile and the pressure tensor for the

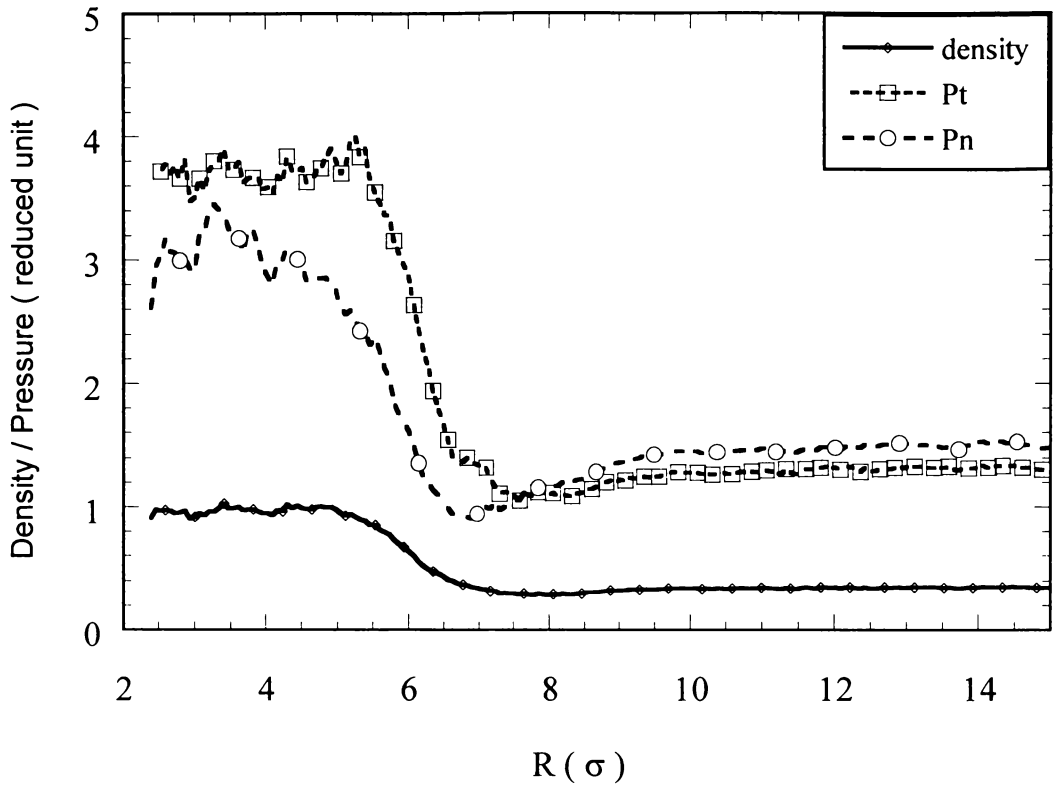


Figure A-3. Density and pressure tensor profiles for the system with surfactant.

system with surfactant. The statistics near the center of the aggregate are very poor; therefore, the data in that region are not shown to avoid confusion. The transverse component of the pressure tensor is seen to be higher than the normal pressure, which is not reasonable because it leads to negative interfacial tension. The cause of this nonphysical result is the cancellation of pair contributions in the calculation of the configurational part of the transverse pressure tensor. This is obviously not adequate, and there is an ongoing effort to find and correct the coding error. On the other hand, the normal component of the pressure tensor gives a reasonable result. It also converges to an average pressure at ~1.5 reduced unit, which is consistent with the average pressure throughout the box at a distance far outside the aggregate. Since the expression and implementation of the normal pressure are more straightforward and judging from the facts provided above, the normal pressure profile is believed to be reliable here, and the transverse pressure profile obtained directly from the simulation is judged to be not reliable. However, by assuming mechanical equilibrium, the normal and transverse components of the pressure tensor can be calculated from each other, and the interfacial tension can be obtained. This is the typical method generally used for determining interfacial tension in simulations for spherical systems. The normal component of the pressure tensor obtained independently from the simulation has been used here for the reasons mentioned above, and the transverse component has been calculated from it.

As a comparison, the same calculation has also been implemented for the system without surfactant, and figure A-4 shows the results. Again, the transverse component

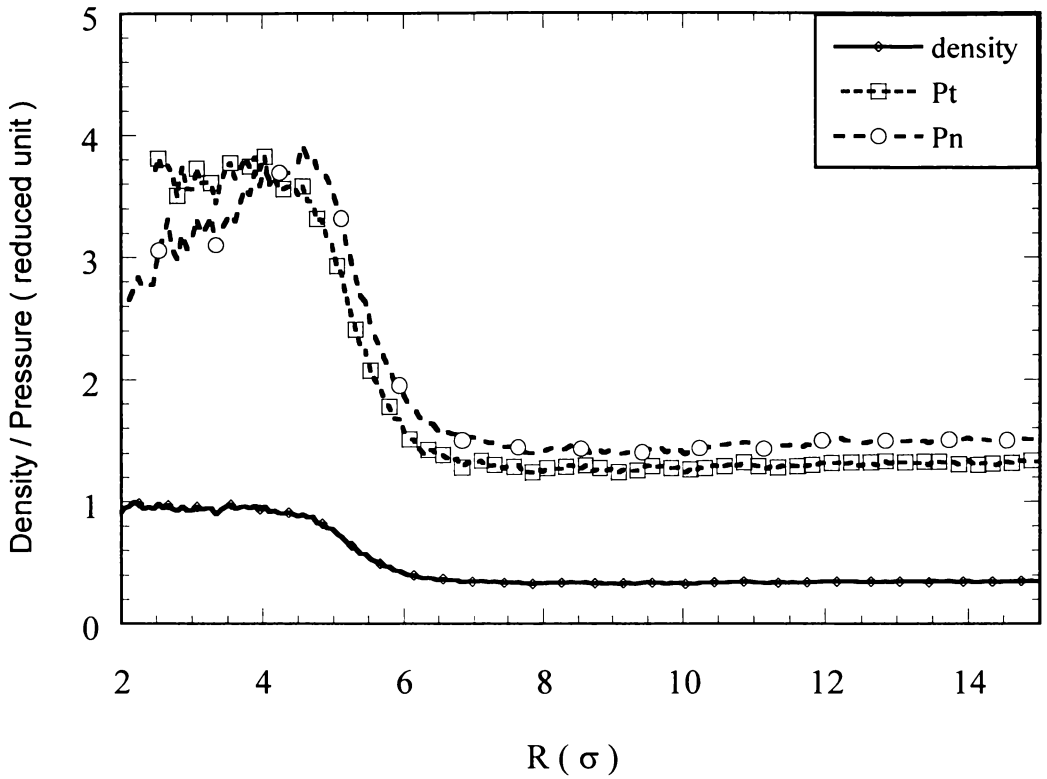


Figure A-4. Density and pressure tensor profiles for system without surfactant.

appears to be erroneous. However, a qualitative difference is seen between the normal pressure tensor components of the system with surfactant and without surfactant. Figure A-5 compares both of the normal component of the pressure tensor from systems with and without surfactant. In the figure, there is a local maximum in the interfacial region for the system without surfactant. This may due to the repulsion between carbon dioxide and water molecules. For the system with surfactant, the local maximum is not so obvious and the pressure is clearly reduced at the same region due to the presence of the surfactant that stabilizes the interface by the attractive interactions between water and head and carbon dioxide and tail.

Figures A-6 and A-7 show the normal component of the pressure tensor from simulation and the transverse component calculated from it. The function used to fit the normal pressure profile is a 9^{th} order polynomial function within the interfacial region, and is set to be equal to P_n outside the region. For the system with surfactant, the transverse pressure profile first goes down and reaches a minimum at $R \sim 6\sigma$, and then goes up through a small local maximum before converging to the normal pressure profile. For the system without surfactant, the transverse pressure profile first goes up due to the local maximum in the normal pressure, and then goes through a profile similar to that of the system with surfactant. However, there is no local maximum at the outer side of the interfacial region because the normal pressure profile does not go through a local minimum at the interface.

The difference between the normal and transverse pressure profiles can then be

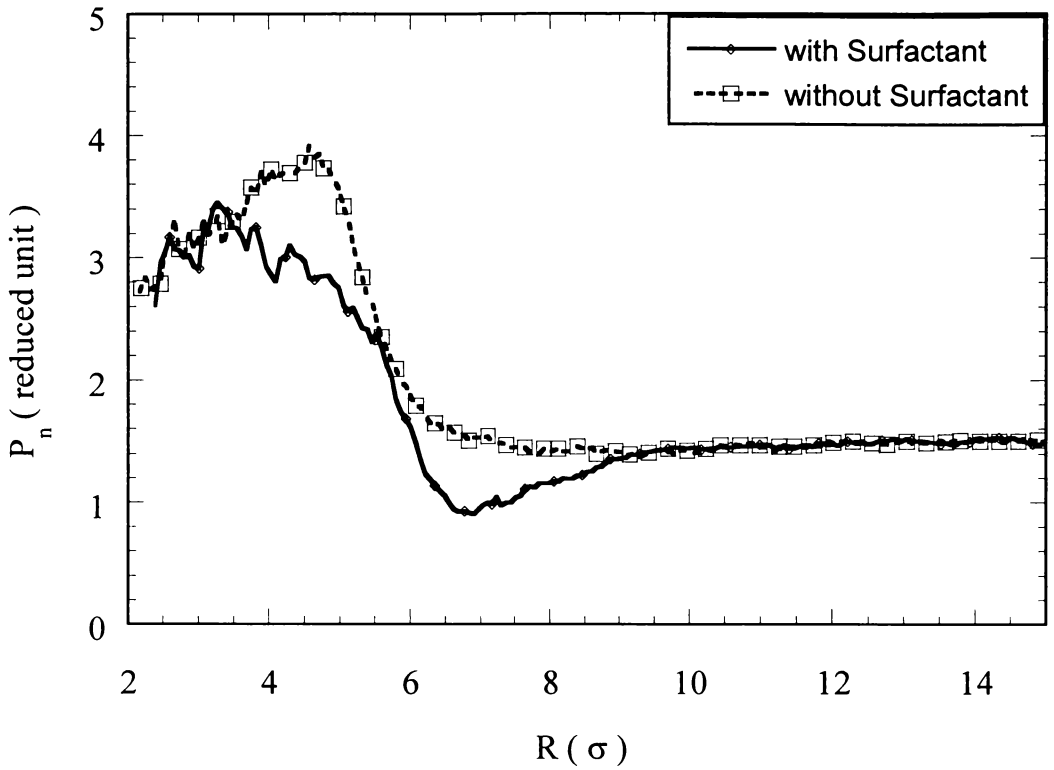


Figure A-5. Comparison of P_n pressure profile for systems with and without surfactant.

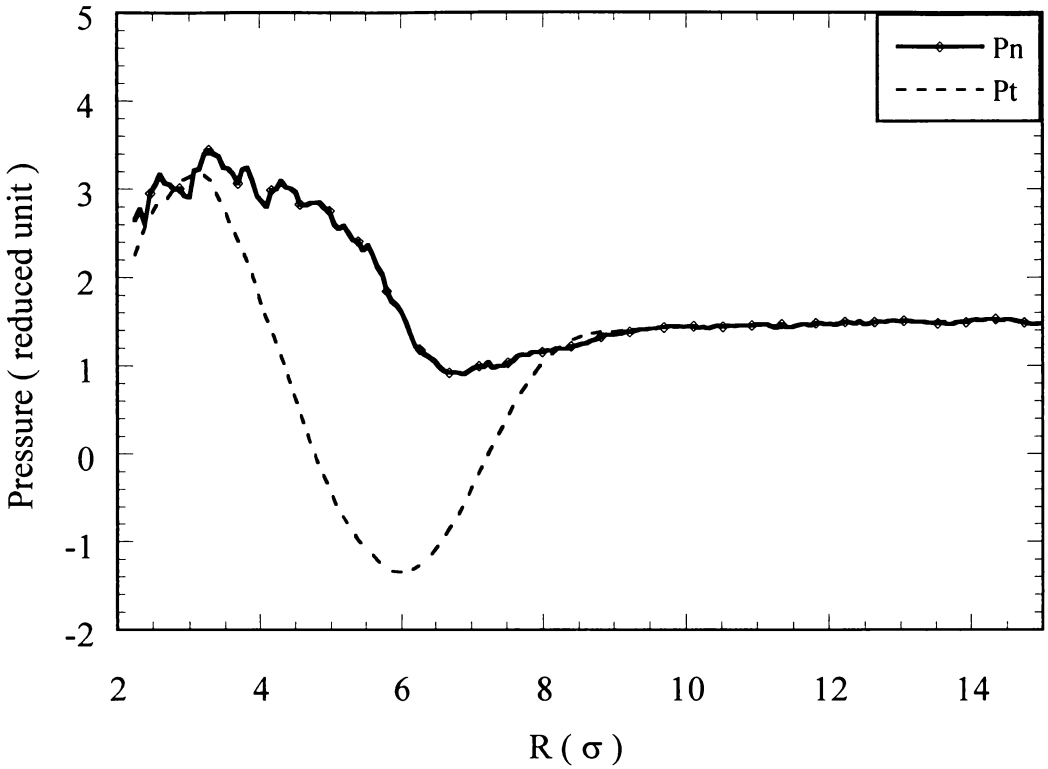


Figure A-6. P_n pressure profile from simulation and Pt calculated from Pn for systems with surfactant.

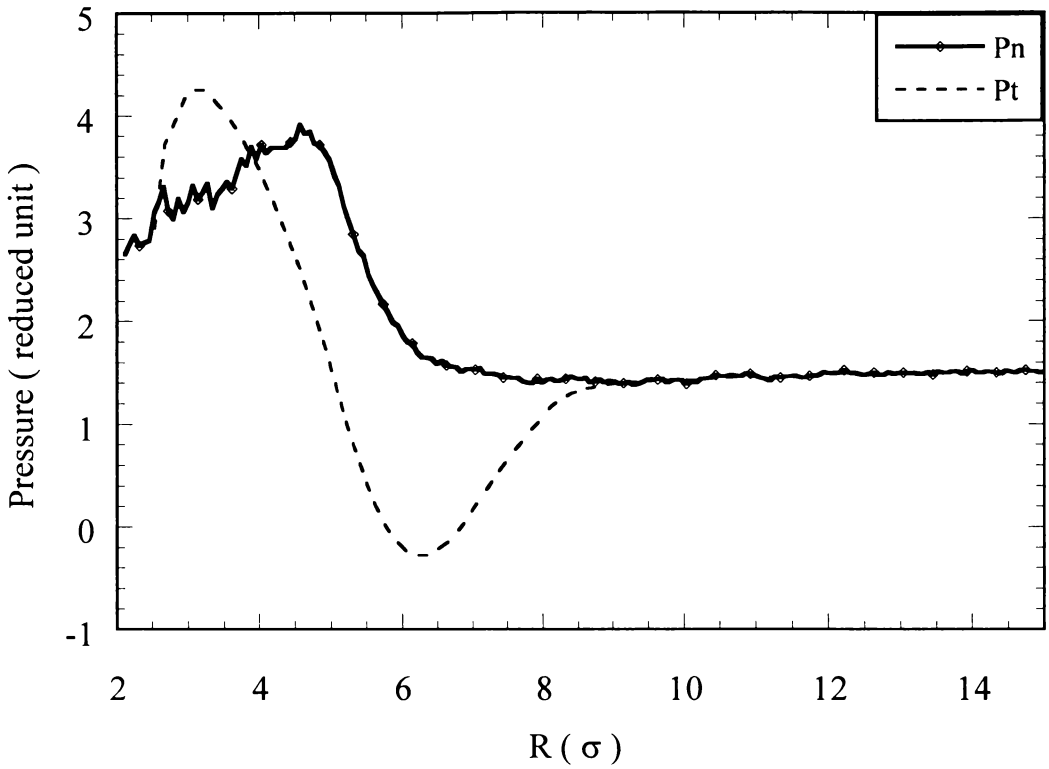


Figure A-7. P_n pressure profile from simulation and Pt calculated from Pn for systems without surfactant.

used with equations A-5 and A-6 to calculate the interfacial tension. The calculated interfacial tension is 55.96 dyne/cm for the system with surfactant and 54.45 dyne/cm for the system without surfactant, which presents no significant difference even though the normal pressure profiles are clearly qualitatively different. Even though the magnitude of the calculated interfacial tension appears to be approximately correct, it does not seem reasonable that the interfacial tension of the system with surfactant is not significantly lower than that of the system without surfactant. Thus, there remain unanswered questions about the validity of the results presented in this appendix.

A.4 Conclusions and recommendations for the reverse micelle work

The density and normal pressure profiles have been obtained from the simulation and the transverse pressure profile has been derived from the normal pressure profile by assuming mechanical equilibrium. A qualitative difference in the normal pressure profile is observed between systems with and without surfactant. However, the interfacial tension obtained from the pressure profiles for both systems do not show significant difference. The effort to obtain the transverse pressure profile independently from simulation is still ongoing, and it is hoped to clarify the ambiguity.

One of the interesting applications for such a reverse micelle system is to use it as a reaction medium for numerous types of reactions such as enzymatic reactions. Therefore, it will be interesting to put potential reactant molecules in the water core and study their properties such as geometry conformations inside the core and compare them to those with the reactants in bulk water.

Because of the already very large size of the system, it is highly unlikely to carry out a simulation with more then one aggregate at this atomistic level. It will also be interesting to develop a coarse-grained model of the system and simulate the system with a much larger size, which can provide better statistics for the study and also make the simulation of the real application possible.

Specific recommendations for further work are as follows:

1. Carry out grand canonical Monte Carlo simulation for the reverse micelle system to check whether the system reaches equilibrium.
2. Refine the calculation of the pressure tensor.
3. Simulate the system with a more coarse-grained model which will allow the simulation to be carried out for larger system size.
4. Simulation with interesting molecules in the water core.
5. Simulate the reverse micelle system with perfluoroethers as surfactant.

APPENDIX B

IMPLEMENTATION AND APPLICATION OF GIBBS-DUHEM INTEGRATION

In this work the Gibbs-Duhem integration technique [48] has been extended for the simultaneous optimization of several interaction parameters of several similar compounds. The case illustrated here and used in this work is for parameters of Lennard-Jones sites in molecular fluids.

For a state function, M, the change of M can be described by the total differential of M as follows:

$$dM = \frac{\partial M}{\partial a_1} da_1 + \frac{\partial M}{\partial a_2} da_2 + ... \tag{B-1}$$

where a_i stands for a set of independent variables and $M = M(a_1, a_2, ...)$.

For a thermodynamic system, the change of total Gibbs free energy, $n\underline{G} = n\underline{G}(P, T, s, n_1, n_2, ...)$, can be expressed as:

$$dn\underline{G} = \left(\frac{\partial n\underline{G}}{\partial T}\right) dT + \left(\frac{\partial n\underline{G}}{\partial P}\right) dP + \sum \left(\frac{\partial n\underline{G}}{\partial n_i}\right) dn_i + \left(\frac{\partial n\underline{G}}{\partial s}\right) ds \tag{B-2}$$

where s is a particular independent variable other than temperature T, pressure P, and number of moles, n_i, of each component. The partial differentiation is only with respect to the corresponding independent variable, with the other variables being held constant.

Also the basic thermodynamic equation gives

$$n\underline{G} = \sum n_i \mu_i \tag{B-3}$$

where μ is the chemical potential. The total differentiation of equation B-3 gives:

$$dn\underline{G} = \sum \left(n_i d\mu_i + \mu_i dn_i \right) \tag{B-4}$$

Combining equations B-2 and B-4 and applying to pure fluid, one has:

$$nd\mu = \left(\frac{\partial n\underline{G}}{\partial T} \right) dT + \left(\frac{\partial n\underline{G}}{\partial P} \right) dP + \left(\frac{\partial n\underline{G}}{\partial s} \right) ds \tag{B-5}$$

Note that this is just the Gibbs-Duhem equation for a pure fluid with an extra independent variable. If one is interested in the correlation between P and T, then equation B-5 will lead to the basic equation for Gibbs-Duhem integration, the Clapeyron equation.

Now, assuming that one is interested in the correlation between T and s as an independent variable for the potential energy, and keeping P and n constant:

$$d\mu = \left(\frac{\partial \underline{G}}{\partial T} \right) dT + \frac{1}{n} \left(\frac{\partial n\underline{G}}{\partial s} \right) ds \tag{B-6}$$

in which,

$$\left(\frac{\partial \underline{G}}{\partial T} \right)_{P,n,s\ldots} = -\underline{S} \tag{B-7}$$

assuming $n\underline{G}$ can be given as $\beta\, n\underline{G} = -\ln Q$ where Q is the partition function; in this case $Q = \int \exp[-\beta U(s)]$. Then, one has

$$\left(\frac{\partial \beta\, n\underline{G}}{\partial s} \right) = -\frac{1}{Q} \frac{\partial Q}{\partial s} = \left\langle \frac{\partial (\beta U)}{\partial s} \right\rangle \tag{B-8}$$

Let $\underline{D}s = \frac{1}{n}\left(\frac{\partial n\underline{G}}{\partial s}\right)$ and write down the equation for two phases.

$$d\mu_\alpha = -\underline{S}_\alpha dT + \underline{D}_{s\alpha} ds \tag{B-9}$$

$$d\mu_\beta = -\underline{S}_\beta dT + \underline{D}_{s\beta} ds \tag{B-10}$$

Along the equilibrium line, $d\mu_\alpha$ should equal to $d\mu_\beta$; therefore

$$-\underline{S}_\alpha dT + \underline{D}_{s\alpha} ds = -\underline{S}_\beta dT + \underline{D}_{s\beta} ds \tag{B-11}$$

Rearranging equation B-11 gives:

$$\left(\frac{dT}{ds}\right)_{eq.} = \frac{\Delta \underline{D}_s}{\Delta \underline{S}} \tag{B-12}$$

For a reversible process such as an equilibrium phase transition, $\Delta S = \Delta H/T$, and equation (B-12) becomes:

$$\left(\frac{dT}{ds}\right)_{eq.} = \frac{\Delta \underline{D}_s}{\Delta \underline{H}/T} \tag{B-13}$$

Now, $\underline{D}_s$ is needed. For the Lennard Jones pair potential

$$\begin{aligned} U = &\frac{1}{2}\sum_i \sum_{j\neq i} \sum_m \sum_n 4\varepsilon_{mn}\left[\left(\frac{\sigma_{mn}}{r}\right)^{12} - \left(\frac{\sigma_{mn}}{r}\right)^{6}\right] \quad \text{- inter} \\ &+ \frac{1}{2}\sum_i \sum_m \sum_{|m-n|\geq 4} 4\varepsilon_{mn}\left[\left(\frac{\sigma_{mn}}{r}\right)^{12} - \left(\frac{\sigma_{mn}}{r}\right)^{6}\right] \quad \text{- intra} \end{aligned} \tag{B-14}$$

Note that the potential energy normally contains the contributions from other sources such as the electrostatic potential and bonding potentials like bending and torsional potentials. However, those interactions are independent of any change in ε and σ; therefore, they are neglected here. Since the summation in equation B-14 is only

important during the code implementation, the focus here is on the potential itself. One needs to know the effect of both ε and σ on the temperature shift.

For a particular energy parameter ε_t

$$\begin{aligned}\frac{\partial U}{\partial \varepsilon_t} &= 4\cdot\frac{\partial}{\partial \varepsilon_t}\left\{(\varepsilon_m\varepsilon_n)^{1/2}\left[\left(\frac{\sigma_m^6\sigma_n^6}{r^{12}}\right)-\left(\frac{\sigma_m^3\sigma_n^3}{r^6}\right)\right]\right\}\\ &= 4\cdot\frac{1}{2}\cdot\left\{(\varepsilon_m\varepsilon_n)^{-1/2}\left[\left(\frac{\sigma_m^6\sigma_n^6}{r^{12}}\right)-\left(\frac{\sigma_m^3\sigma_n^3}{r^6}\right)\right]\right\}\left(\varepsilon_m\frac{\partial\varepsilon_n}{\partial\varepsilon_t}+\varepsilon_n\frac{\partial\varepsilon_m}{\partial\varepsilon_t}\right)\left(\frac{\varepsilon_m\varepsilon_n}{\varepsilon_m\varepsilon_n}\right)\\ &= 2\cdot\left\{(\varepsilon_m\varepsilon_n)^{1/2}\left[\left(\frac{\sigma_m^6\sigma_n^6}{r^{12}}\right)-\left(\frac{\sigma_m^3\sigma_n^3}{r^6}\right)\right]\right\}\left(\frac{1}{\varepsilon_n}\frac{\partial\varepsilon_n}{\partial\varepsilon_t}+\frac{1}{\varepsilon_m}\frac{\partial\varepsilon_m}{\partial\varepsilon_t}\right)\end{aligned} \quad \text{(B-15)}$$

where geometric mean combining rules have been used for $\varepsilon_{mn}=(\varepsilon_m\varepsilon_n)^{1/2}$ and $\sigma_{mn}=(\sigma_m\sigma_n)^{1/2}$. Since reduced units are used in the code, the part of the equation that is calculated in the loop of simulation code needs to be transformed into reduced units.

$$\frac{\partial U}{\partial \varepsilon_t} = 2\cdot\left\{(\varepsilon_m^*\varepsilon_n^*)^{1/2}\left[\left(\frac{\sigma_m^{*6}\sigma_n^{*6}}{r^{*12}}\right)-\left(\frac{\sigma_m^{*3}\sigma_n^{*3}}{r^{*6}}\right)\right]\right\}\cdot\varepsilon_R\cdot\left(\frac{1}{\varepsilon_n}\frac{\partial\varepsilon_n}{\partial\varepsilon_t}+\frac{1}{\varepsilon_m}\frac{\partial\varepsilon_m}{\partial\varepsilon_t}\right) \quad \text{(B-16)}$$

where ε_R is the reference energy parameter.

For a particular size parameter, σ_t:

$$\begin{aligned}\frac{\partial U}{\partial \sigma_t} &= 4\cdot\frac{\partial}{\partial \sigma_t}\left\{(\varepsilon_m\varepsilon_n)^{1/2}\left[\left(\frac{\sigma_m^6\sigma_n^6}{r^{12}}\right)-\left(\frac{\sigma_m^3\sigma_n^3}{r^6}\right)\right]\right\}\\ &= 4\cdot(\varepsilon_m\varepsilon_n)^{1/2}\cdot\frac{\partial}{\partial \sigma_t}\left\{\left[\left(\frac{\sigma_m^6\sigma_n^6}{r^{12}}\right)-\left(\frac{\sigma_m^3\sigma_n^3}{r^6}\right)\right]\right\}\end{aligned}$$

$$= 4 \cdot (\varepsilon_m \varepsilon_n)^{1/2} \cdot \left\{ \begin{array}{l} \left(6 \frac{\sigma_m^5 \sigma_n^6}{r^{12}} \frac{\partial \sigma_m}{\partial \sigma_t} \cdot \frac{\sigma_m}{\sigma_m} + 6 \frac{\sigma_m^6 \sigma_n^5}{r^{12}} \frac{\partial \sigma_n}{\partial \sigma_t} \cdot \frac{\sigma_n}{\sigma_n} \right) \\ - \left(3 \frac{\sigma_m^2 \sigma_n^3}{r^6} \frac{\partial \sigma_m}{\partial \sigma_t} \cdot \frac{\sigma_m}{\sigma_m} + 3 \frac{\sigma_m^3 \sigma_n^2}{r^6} \frac{\partial \sigma_n}{\partial \sigma_t} \cdot \frac{\sigma_n}{\sigma_n} \right) \end{array} \right\}$$

$$= 4 \cdot (\varepsilon_m \varepsilon_n)^{1/2} \cdot \left\{ \begin{array}{l} \left(6 \frac{\sigma_m^6 \sigma_n^6}{r^{12}} \frac{\partial \sigma_m}{\sigma_m \partial \sigma_t} + 6 \frac{\sigma_m^6 \sigma_n^6}{r^{12}} \frac{\partial \sigma_n}{\sigma_n \partial \sigma_t} \right) \\ - \left(3 \frac{\sigma_m^3 \sigma_n^3}{r^6} \frac{\partial \sigma_m}{\sigma_m \partial \sigma_t} + 3 \frac{\sigma_m^3 \sigma_n^3}{r^6} \frac{\partial \sigma_n}{\sigma_n \partial \sigma_t} \right) \end{array} \right\}$$

$$= 4 \cdot (\varepsilon_m \varepsilon_n)^{1/2} \cdot \left\{ \left(6 \frac{\sigma_m^6 \sigma_n^6}{r^{12}} \right) - \left(3 \frac{\sigma_m^3 \sigma_n^3}{r^6} \right) \right\} \cdot \left(\frac{\partial \sigma_m}{\sigma_m \partial \sigma_t} + \frac{\partial \sigma_n}{\sigma_n \partial \sigma_t} \right)$$

$$= 4 \cdot (\varepsilon_m \varepsilon_n)^{1/2} \cdot \left\{ \left(6 \frac{\sigma_m^6 \sigma_n^6}{r^{12}} \right) - \left(3 \frac{\sigma_m^3 \sigma_n^3}{r^6} \right) \right\} \cdot \left(\frac{\partial \sigma_m}{\sigma_m \partial \sigma_t} + \frac{\partial \sigma_n}{\sigma_n \partial \sigma_t} \right) \qquad \text{(B-17)}$$

Again, one needs to use reduced units in part of the expression to go with the code.

$$\frac{\partial U}{\partial \sigma_t} = 4 \cdot \left\{ \left(\varepsilon_m^* \varepsilon_n^* \right)^{1/2} \left[6 \left(\frac{\sigma_m^{*6} \sigma_n^{*6}}{r^{*12}} \right) - 3 \left(\frac{\sigma_m^{*3} \sigma_n^{*3}}{r^{*6}} \right) \right] \right\} \cdot \varepsilon_R \cdot \left(\frac{\partial \sigma_m}{\sigma_m \partial \sigma_t} + \frac{\partial \sigma_n}{\sigma_n \partial \sigma_t} \right) \qquad \text{(B-18)}$$

The calculations can be carried out along with the calculation of the LJ interaction energy in the simulation, and then the ensemble average can be taken to give $\underline{D_s}$ for both phases with respect to different size and energy parameters.

With equations B-16 and B-18, the step-by-step procedure to optimize the Lennard-Jones parameters is as follows:

1. Carry out Gibbs ensemble Monte Carlo simulation with a predetermined set of Lennard-Jones parameters and equations B-16 and B-18 implemented. This should be done on a temperature at the middle of the phase envelope for all

compounds if only one set of simulations is planned for each compound. From this $\Delta\underline{D}_s$ at this temperature can be obtained.

2. Obtain the system pressure and saturated molar volumes for each phase diagram, and hence the $\Delta\underline{H}$.

3. Calculate the shift of equilibrium temperature due to the parameter changes by equation B-13. A set of optimized parameters can be obtained by adjusting the equilibrium temperature to the experimental phase envelopes for all the compounds.

4. Based on the newly calculated state point from step 3, use regular P-T Gibbs-Duhem integration [89] to obtain the whole phase diagram. If the phase envelope is satisfactory, proceed to step 5. If not, use the set of parameters obtained in step 3 as the pre-selected set of parameters and go back to step 1.

5. Do Gibbs ensemble Monte Carlo on each data point on every phase diagram to test the actual performance of the parameter set. In step 1, molecular simulation is carried out only at one equilibrium temperature, and this may be the reason for non-convergence of the procedure if it does happen. In this case, step 1 needs to be done at several different temperatures along the coexistence line and dT/ds between two designated temperatures should be interpolated. Another possible reason for non-convergence may be the complexity of the contours with respect to the Lennard-Jones parameters. In this case, a limit of maximum parameter changes in step 3 should be set, and more iterations may be necessary to achieve the final optimized set of parameters.

VITA

Hung-Chih Li was born in Taipei, Taiwan on October 2, 1971. He went to high school at Chen-Kuo senior high school in Taipei and graduated in 1990. He went to National Taiwan University and received a B.S. in chemical engineering in 1994. After that, he served in the Army for two years for a mandatory military service. He then went to the University of Tennessee, Knoxville and received a M.S. in chemical engineering in 1998.

Hung-Chih is currently pursuing his doctorate in chemical engineering at the University of Tennessee, Knoxville, TN.

3238 2553 47
07-24-02 MAB